AIAA JOURNAL
Vol. 49, No. 1, January 2011

Numerical Investigation of Wave Packets in a Mach 3.5 Cone Boundary Layer

Christian S. J. Mayer,* Andreas C. Laible,† and Hermann F. Fasel‡
University of Arizona, Tucson, Arizona 85721

DOI: 10.2514/1.J050038

Transition initiated by a wave packet in a cone boundary layer at Mach 3.5 has been investigated using linear stability theory and direct numerical simulations. Disturbances have been introduced into the boundary layer by pulsing the wall-normal velocity through a hole on the cone surface. The present study can be divided into three parts. In the first part, the linear development of a wave packet is studied in detail. The second part focuses on the identification of possible, asymmetric resonance triads for the most dominant oblique instability waves of the wave packet. New triads have been found that have not yet been reported for a supersonic boundary layer. These triads might explain some major findings in the third part of the present work, which focuses on the weakly nonlinear development of a wave packet that was generated by a large-amplitude pulse. The initial disturbance development of this wave packet remains still linear, while farther downstream nonlinear wave interactions alter the shape and the disturbance spectrum of the packet. The results of the third part suggest that oblique breakdown might be the strongest nonlinear transition mechanism for a supersonic boundary layer.

Nomenclature

A	=	disturbance amplitude
c	=	speed of sound
c_p	=	specific heat at constant pressure
E_t	=	total energy
F	=	reduced frequency
f	=	frequency
i	=	$\sqrt{(-1)}$
k	=	thermal conductivity
k_c	=	azimuthal mode number
L	=	arbitrary reference length
M	=	Mach number
Pr	=	Prandtl number
p	=	pressure
$\boldsymbol{q}$	=	heat flux vector
Re	=	global Reynolds number
R_x	=	local Reynolds number
r	=	radius
r_{nose}	=	cone nose radius
T	=	temperature, period
t	=	time
u, v, w	=	velocity components
x, y, φ	=	coordinates
x_0, x_L	=	location of inflow, outflow
x_1, x_2	=	start, end of disturbance hole in x
y_H	=	domain height
z	=	azimuthal coordinate on the unrolled cone surface
z_1, z_2	=	start, end of disturbance hole in z

Greeks

$-\alpha_i$	=	streamwise amplification rate
α_r, β	=	streamwise azimuthal wave number
γ	=	ratio of specific heats
δ	=	boundary-layer thickness
θ	=	phase in streamwise direction
θ_c	=	cone half angle
λ	=	wavelength
μ	=	dynamic viscosity
ν	=	kinematic viscosity
ρ	=	density
σ	=	factor to determine degree of upwinding
τ_{ij}	=	stress tensor
ω	=	angular frequency

Subscripts

$[n, k]$	=	modes in time, spanwise direction
w	=	wall
∞	=	approach flow conditions

Superscripts

1	=	primary wave of a triad
2, 3	=	secondary waves of a triad
*	=	dimensional value
$'$	=	disturbance value

Presented as Paper 2009-3809 at the 39th AIAA Fluid Dynamics Conference, San Antonio, TX, 22–25 June 2009; received 18 August 2009; revision received 26 July 2010; accepted for publication 10 August 2010.

*Department of Aerospace and Mechanical Engineering; currently at ExxonMobil Upstream Research Company, Houston, TX 77252. Member AIAA.

†Research Assistant, Department of Aerospace and Mechanical Engineering. Member AIAA.

‡Professor, Department of Aerospace and Mechanical Engineering. Member AIAA.

I. Introduction

THE transition process, especially the nonlinear regime, in supersonic boundary layers for a sharp cone is far from being understood. A large number of investigations have been performed for the flat-plate geometry at supersonic speeds with the focus on different nonlinear transition scenarios [1–7]. One transition scenario is the so-called oblique breakdown mechanism initiated by two oblique instability waves with equal but opposite wave angle. This mechanism was first discovered for a supersonic flat-plate boundary layer at Mach 1.6 by Thumm [8] and Fasel et al. [1]. The second mechanism is termed *asymmetric subharmonic resonance* and was first observed in the experiments by Kosinov et al. [9] for a flat-plate boundary layer at Mach 2. In this resonance mechanism, one oblique fundamental wave interacts with two oblique (asymmetric) subharmonic waves forming a so-called resonance triad.

For a sharp cone, only a few numerical and experimental studies exist. The first linear stability calculations for a sharp cone boundary layer were conducted by Malik [10], Mack [11], and Gasperas [12]. These authors did not account for the streamwise boundary-layer growth and therefore, for nonparallel effects in their stability analysis. Malik [10] investigated a supersonic boundary layer on a sharp cone (5° half angle) at zero angle of attack at various Mach numbers. He did not consider the curvature terms for the calculation of the mean flow profiles and the eigenvalue analysis. The mean flow conditions for his calculations matched the flight experiments from Fisher and Dougherty [13] (Mach 1.2, 1.35, 1.6 and 1.92) and the quiet tunnel experiments from Beckwith et al. [14] at Mach 3.5 (before shock). Malik [10] showed that in these low freestream disturbance experiments, transition could be predicted by the e^N method with N ranging from 9 to 11. The experimental and numerical studies by Chen et al. [15,16] for a sharp cone and a flat-plate at Mach 3.5 confirmed this statement.

All the investigations for a cone mentioned preceding did not focus on a particular transition scenario and therefore, also not on the nonlinear transition regime. In the experiments by Beckwith et al. [14] and Chen et al. [16] for a sharp cone at Mach 3.5, the authors did not monitor the development of a single instability wave or identify a particular breakdown mechanism. Their focus had been on the determination of the transition location and the corresponding transition Reynolds number. The controlled experiments by Corke et al. [17] and Matlis [18] for a sharp cone at Mach 3.5 (half angle 7°) at NASA Langley are the only experiments that have studied a particular transition route. They observed an asymmetric subharmonic resonance where the fundamental and subharmonic waves have the same azimuthal mode number.

In the experimental studies by Corke et al. [17] and Matlis [18], the boundary layer was perturbed periodically by using an azimuthal array of 24 disturbance actuators based on a glow discharge. With this setup the experimentalists were able to excite a pair of instability waves at a particular frequency and equal but opposite wave angles. Experiments of such nature are very important and play a vital role in validating theoretical results for both the linear and the nonlinear transition regime. However, they only provide limited insight into a natural transition scenario where a broad disturbance spectrum is excited by freestream disturbances and where complex wave interactions between all disturbance modes are possible.

The focus of the present work is therefore to investigate transition initiated by a broad disturbance spectrum. To excite a wide range of disturbance waves, a wave packet is generated by a pulse through a hole on the cone surface. In the past, this approach was also used for incompressible boundary layers [19–22]. The streamwise development of the wave packet is studied in detail for the linear and weakly nonlinear regime. Furthermore, using linear stability theory (LST) [23] subharmonic resonance triads and several new resonance triads are identified that might explain the weakly nonlinear disturbance development observed in the disturbance spectra of the wave packet obtained from the computed wall pressure.

II. Simulation Setup

A. Physical Problem and Computational Setup

Supersonic flow at Mach 3.5 over a cone is investigated numerically using spatial direct numerical simulations (DNS). The computational setup follows the experimental study by Corke et al. [17] and Matlis [18] at the NASA Langley Quiet Wind Tunnel and the numerical investigations by Laible et al. [24]. The cone has a semivertex angle of $\theta_c = 7°$, and a cone length of $L^* = 0.3556$ m. The nose radius of the cone is given as $r^*_{\text{nose}} = 0.038$ mm. The cone can be considered as sharp because the entropy layer is swallowed by the boundary layer about 4 mm ($R_x = 213$, with R_x as local Reynolds number defined as $R_x = \sqrt{\frac{U^*_\infty x^*}{\nu^*_\infty}}$) downstream of the nose tip and therefore, upstream of the unstable region which starts at about $R_x \sim 325$ (for an azimuthal mode number $k_c = 5$). The approach flow of the experiments in the NASA Quiet Wind Tunnel had a Mach number of 3.8 and a unit Reynolds number of 9.45×10^6 m^{-1}. The stagnation temperature and pressure were given as 310.9 K and 1.724×10^5 Pa, respectively. The cone wall of the experiments can be assumed to be adiabatic with respect to the steady mean flow and isothermal with respect to the high-frequency disturbances of the wave packet. Throughout this paper all DNS are performed for these conditions. A schematic of the cone model and the corresponding coordinate system for all simulations is shown in Fig. 1.

As initial condition for the simulations of the wave packet, mean flow results from earlier simulations [24] have been interpolated and converged onto a new computational grid. The entire procedure to obtain an accurate mean flow solution for the conical geometry is explained in detail in Laible et al. [24]. The computational domain for all simulations in this paper starts at $x^*_0 = 0.105$ m and thus, does not include the nose tip. The outflow is positioned at $x^*_L = 0.327$ m. The domain height is chosen as $y^*_H = 0.075$ m, which corresponds to about 80 boundary layer thicknesses δ at the outflow. In azimuthal direction, only one third of the cone is simulated. The azimuthal domain extent is set according to the spreading of the wave packet so that the wave packet cannot reach the azimuthal boundaries while it travels downstream.

The streamwise resolution was determined using linear stability considerations. More details on the flow parameters used for the stability analysis can be found in the succeeding sections. Figures 2a and 2b show an estimate of the streamwise wave length λ_x from LST as a function of reduced frequency $F = 2\pi \frac{f^* \nu^*_\infty}{U^{*2}_\infty}$, local Reynolds number R_x, and azimuthal mode number k_c. Note that the azimuthal mode number is a measure for the azimuthal wave length λ_z of a disturbance. A disturbance with an azimuthal mode number k_c has an azimuthal wave length corresponding to

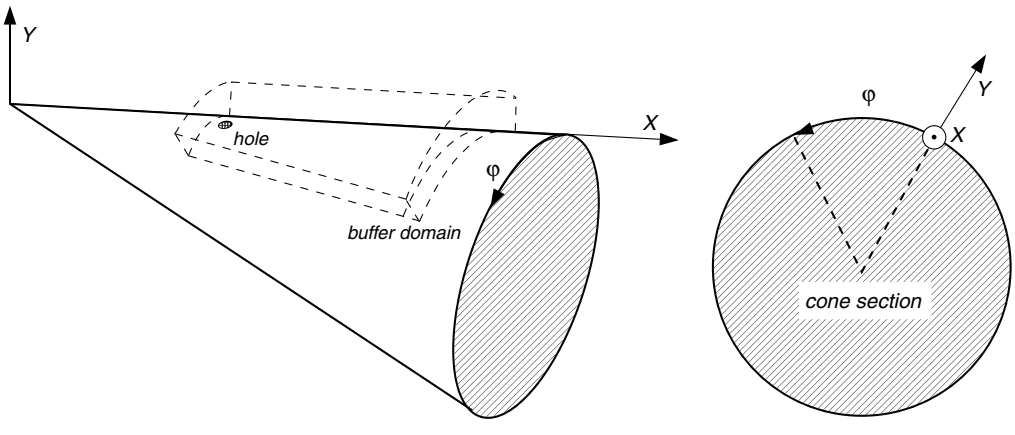

Fig. 1 Cone model used for the NASA experiments: a) three-dimensional view and b) cross section. The sharp cone has a nose radius of 0.038 mm, the semivertex angle is 7° and the model length is 0.3556 m.

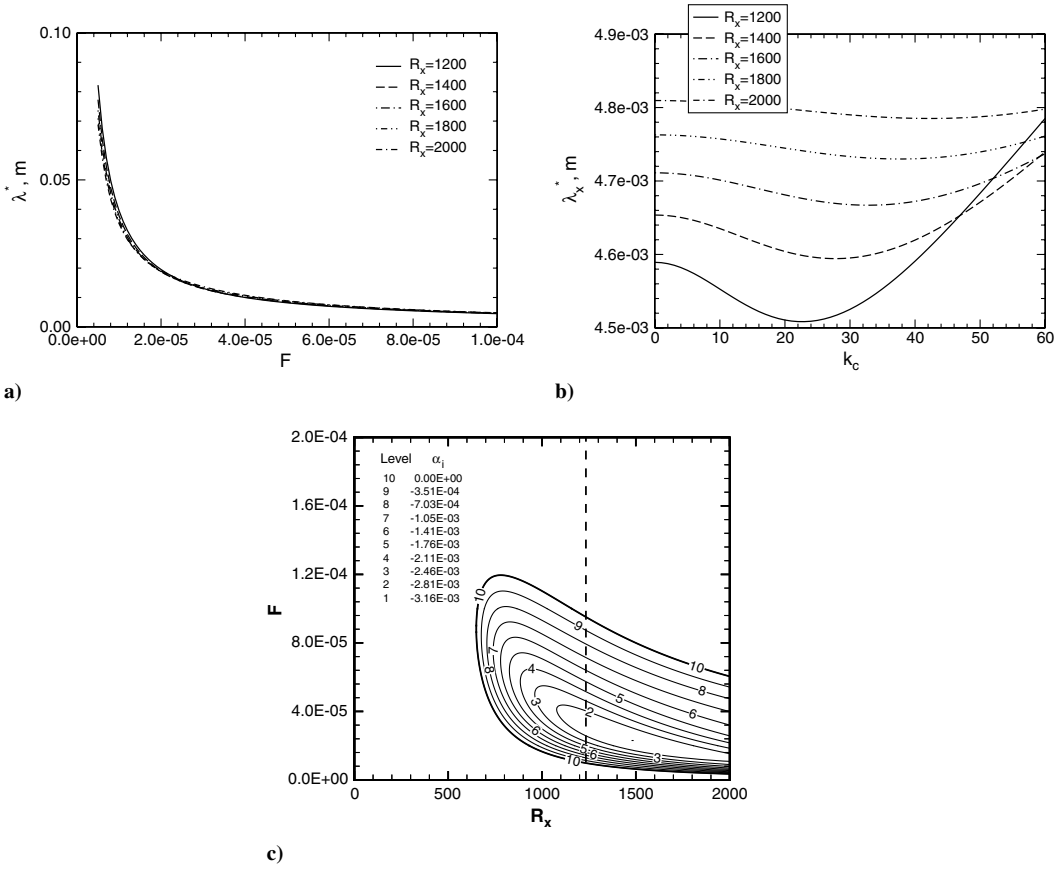

Fig. 2 Estimation of the streamwise wave length λ_x for disturbances included in the wave packet using LST [43]: a) streamwise wave length λ_x as a function of reduced frequency F for azimuthal mode number $k_c = 21$, b) streamwise wave length λ_x as a function of azimuthal mode number for frequency $F = 10^{-4}$, and c) linear stability diagram for azimuthal mode number $k_c = 21$ indicating the forcing location (dashed line).

$$\lambda_z = \frac{2\pi r(x)}{k_c} \tag{1}$$

at the streamwise position x.

Laible et al. [25] report that the most critical disturbances for transition (based on N-factor calculations with $N = 8.5$) on a cone at Mach 3.5 have a frequency of about 2.0×10^{-5} and an azimuthal mode number of $k_c = 32$. Hence, a disturbance band with $F = 10^{-4}$ as the highest disturbance frequency should include the most dominant frequencies for a wave packet on a cone at Mach 3.5. From Figs. 2a and 2b, it can be concluded that disturbances with frequency $F = 10^{-4}$ have the smallest streamwise wave length for $k_c = 21$ at $R_x = 2000$ ($\simeq$ the end of the cone). This wave length has a dimensional value of about 0.0045 m and is resolved by 10 points in all simulations discussed in this paper. In wall-normal direction, two grids with a fine resolution and coarse resolution have been used. For the fine grid, the boundary layer is resolved by about 33 points at the inflow and about 50 points at the outflow while for the coarse grid the wall resolution is reduced to about 44 points at the outflow. Additionally, the wall-normal grid for both cases is stretched in order to stabilize the numerical scheme as discussed in Sec. II.C. The overall number of grid points for the fine wall-normal resolution is 301 whereas for the coarser grid 231 points are used. Pseudospectral discretization was employed in azimuthal direction with about 100 Fourier modes and the flow was assumed to be symmetric to the centerline of the cone. Note that 100 Fourier modes are necessary for the simulations with a high forcing amplitude while for simulations of the linear disturbance regime a smaller number of Fourier modes suffices.

Disturbances have been introduced into the boundary layer by pulsing the wall-normal velocity through a hole on the cone surface. More details on the disturbance generation can be found in Sec. II.D. The simulation setup was validated by comparing mean flow data to previous simulations summarized in Laible et al. [24] and LST. The linear stability results will be discussed in Sec. III.A and here, only the mean flow data are presented. Figure 3a compares the streamwise development of the boundary layer thickness δ in dimensional form for both wall-normal grids to data from Laible et al. [24] and Mangler-transformed flat-plate results [26]. Note that the Mangler transformation states that for identical edge conditions, the cone mean flow profiles at a particular streamwise position can be obtained from flat-plate profiles. This transformation is only valid in regions where the cone radius is much larger than the boundary layer thickness.

Clearly, there is an excellent agreement between all data sets in Fig. 3a. Even for the coarser grid the boundary layer growth is correctly reproduced. Moreover, the wall-normal distribution of the mass flux in Fig. 3b also matches the result from the Mangler-transformed similarity solution at $x^* = 0.251$ m. Hence, the chosen resolution for the simulation of a supersonic boundary layer over a cone for the previously mentioned flow condition is sufficient. Note that for all results discussed in this paper the finer wall-normal resolution is used except for the figures where explicitly the coarser resolution is highlighted (see Sec. III.A).

B. Governing Equations

The governing equations for our high-order accurate transition simulations are the compressible Navier–Stokes equations in conservative variable formulation written in conical coordinates:

$$\frac{\partial \boldsymbol{U}}{\partial t} + \frac{1}{r}\frac{\partial (r(\boldsymbol{E_c} + \boldsymbol{E_d}))}{\partial x} + \frac{1}{r}\frac{\partial (r(\boldsymbol{F_c} + \boldsymbol{F_d}))}{\partial y} + \frac{1}{r}\frac{\partial (\boldsymbol{G_c} + \boldsymbol{G_d})}{\partial \varphi} + \boldsymbol{H} = 0 \tag{2}$$

where x is the downstream coordinate parallel to the cone surface, y is the wall-normal coordinate orthogonal to the cone surface and φ

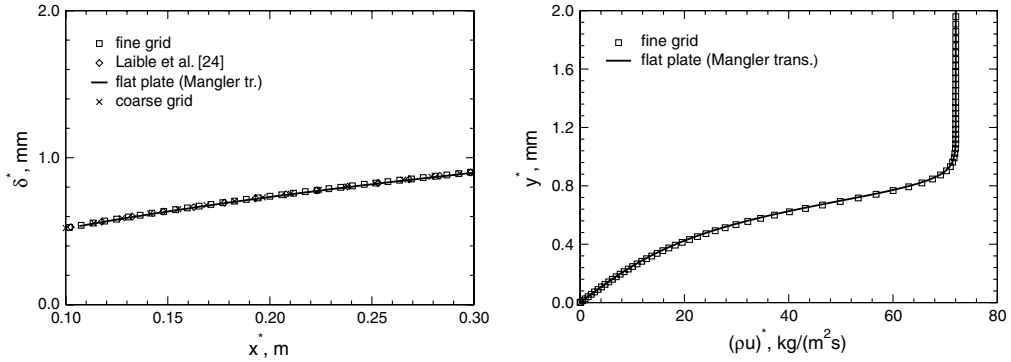

a) b)

Fig. 3 Comparison of selected mean flow properties to previous simulations [24] and flat-plate similarity solution in order to validate the simulation setup (wall-normal grid resolution) for all simulations presented in this paper: a) streamwise development of boundary layer thickness δ and b) wall-normal distribution of mass flux at $x^* = 0.251$ m.

specifies the azimuthal coordinate. The radius r denotes the local radius and is computed according to $r = x\sin\theta_c + y\cos\theta_c$, where θ_c is the half angle (also called semivertex angle) of the cone. The vector of the conservative variables is given as $\boldsymbol{U} = [\rho, \rho u, \rho v, \rho w, E_t]$. The convective flux vectors $(\boldsymbol{E_c}, \boldsymbol{F_c}, \boldsymbol{G_c})$, the viscous and heat conduction terms $(\boldsymbol{E_d}, \boldsymbol{F_d}, \boldsymbol{G_d})$ and the source term $(\boldsymbol{H})$ are

$$\boldsymbol{E_c} = \begin{bmatrix} \rho u \\ \rho u^2 + p \\ \rho uv \\ \rho uw \\ (E_t + p)u \end{bmatrix}, \qquad \boldsymbol{F_c} = \begin{bmatrix} \rho v \\ \rho uv \\ \rho v^2 + p \\ \rho vw \\ (E_t + p)v \end{bmatrix}$$

$$\boldsymbol{G_c} = \begin{bmatrix} \rho w \\ \rho uw \\ \rho vw \\ \rho w^2 + p \\ (E_t + p)w \end{bmatrix}, \qquad \boldsymbol{E_d} = \begin{bmatrix} 0 \\ -\tau_{xx} \\ -\tau_{xy} \\ -\tau_{x\varphi} \\ -u\tau_{xx} - v\tau_{xy} - w\tau_{x\varphi} + q_x \end{bmatrix}$$

$$\boldsymbol{F_d} = \begin{bmatrix} 0 \\ -\tau_{xy} \\ -\tau_{yy} \\ -\tau_{y\varphi} \\ -u\tau_{xy} - v\tau_{yy} - w\tau_{y\varphi} + q_y \end{bmatrix}$$

$$\boldsymbol{G_d} = \begin{bmatrix} 0 \\ -\tau_{x\varphi} \\ -\tau_{y\varphi} \\ -\tau_{\varphi\varphi} \\ -u\tau_{x\varphi} - v\tau_{y\varphi} - w\tau_{\varphi\varphi} + q_\varphi \end{bmatrix}$$

$$\boldsymbol{H} = \begin{bmatrix} 0 \\ -\frac{1}{r}\sin\theta_c(\rho w^2 - \tau_{\varphi\varphi} + p) \\ -\frac{1}{r}\cos\theta_c(\rho w^2 - \tau_{\varphi\varphi} + p) \\ \frac{1}{r}\sin\theta_c(\rho uw - \tau_{x\varphi}) + \frac{1}{r}\cos\theta_c(\rho vw - \tau_{y\varphi}) \\ 0 \end{bmatrix} \tag{3}$$

The total energy is computed as

$$E_t = \rho\left(\frac{T}{(\gamma-1)\gamma M^2} + \frac{1}{2}(u^2 + v^2 + w^2)\right) \tag{4}$$

The stresses in the conical coordinate system are determined by

$$\tau_{xx} = \frac{\mu}{Re}\left(\frac{4}{3}\frac{\partial u}{\partial x} - \frac{2}{3}\frac{\partial v}{\partial y} - \frac{2}{3r}\frac{\partial w}{\partial \varphi} - \frac{2}{3r}(u\sin\theta_c + v\cos\theta_c)\right) \tag{5a}$$

$$\tau_{yy} = \frac{\mu}{Re}\left(\frac{4}{3}\frac{\partial v}{\partial y} - \frac{2}{3}\frac{\partial u}{\partial x} - \frac{2}{3r}\frac{\partial w}{\partial \varphi} - \frac{2}{3r}(u\sin\theta_c + v\cos\theta_c)\right) \tag{5b}$$

$$\tau_{\varphi\varphi} = \frac{\mu}{Re}\left(\frac{4}{3r}\frac{\partial w}{\partial \varphi} - \frac{2}{3}\frac{\partial u}{\partial x} - \frac{2}{3}\frac{\partial v}{\partial y} + \frac{4}{3r}(u\sin\theta_c + v\cos\theta_c)\right) \tag{5c}$$

$$\tau_{xy} = \frac{\mu}{Re}\left(\frac{\partial v}{\partial x} + \frac{\partial u}{\partial y}\right) \tag{5d}$$

$$\tau_{x\varphi} = \frac{\mu}{Re}\left(\frac{1}{r}\frac{\partial u}{\partial \varphi} + \frac{\partial w}{\partial x} - \frac{w\sin\theta_c}{r}\right) \tag{5e}$$

$$\tau_{y\varphi} = \frac{\mu}{Re}\left(\frac{1}{r}\frac{\partial v}{\partial \varphi} + \frac{\partial w}{\partial y} - \frac{w\cos\theta_c}{r}\right) \tag{5f}$$

and the heat flux vector is given as

$$\boldsymbol{q} = -\frac{\mu}{(\gamma-1)RePrM^2}\left(\frac{\partial T}{\partial x}, \frac{\partial T}{\partial y}, \frac{1}{r}\frac{\partial T}{\partial \varphi}\right) \tag{6}$$

The set of equations is closed by the equation of state for a perfect gas:

$$p = \frac{\rho T}{\gamma M^2} \tag{7}$$

The bulk viscosity is set to zero (Stoke's assumption) and the remaining viscosity coefficient μ is calculated using Sutherland's law:

$$\mu = T^{\frac{3}{2}}\frac{1 + \frac{C}{T^*_\infty}}{T + \frac{C}{T^*_\infty}} \tag{8}$$

where $C = 110.4$ K and T^*_∞ represents the dimensional temperature of the approach flow.

The flow quantities are nondimensionalized with their approach flow values, indicated by the subscript ∞, except for the pressure and the total energy, which are scaled by the dynamic pressure $\rho^*_\infty U^{*2}_\infty$. Furthermore, the independent variables x, y and t are nondimensionalized using a reference length scale L^* (and the approach streamwise velocity U^*_∞ for t). The nondimensionalization of the governing equations introduces the Reynolds number Re, Mach

number M, Prandtl number Pr and the ratio of specific heats γ as nondimensional parameters:

$$Re = \frac{\rho^*_\infty U^*_\infty L^*}{\mu^*_\infty}, \qquad Pr = \frac{\mu^*_\infty c^*_{p\infty}}{k^*} = 0.71$$
$$M = \frac{U^*_\infty}{\sqrt{\gamma p^*_\infty / \rho^*_\infty}}, \quad \text{and} \quad \gamma = 1.4 \tag{9}$$

with c, k, c_p being the speed of sound, the thermal conductivity and the specific heat at constant pressure, respectively. The superscript * denotes dimensional quantities.

C. Numerical Scheme

The Navier–Stokes equations are integrated in time with a standard fourth-order accurate Runge–Kutta scheme. The spatial discretization is based on high-order accurate finite differences. In particular, the derivatives of the viscous terms ($\boldsymbol{E_d}, \boldsymbol{F_d}, \boldsymbol{G_d}$) and the source term ($\boldsymbol{H}$) are calculated by up to eighth-order noncompact central differences in the downstream direction and up to eighth-order noncompact central differences in wall-normal direction. In the azimuthal direction, the code has the option between up to 10th-order accurate compact differences and a pseudospectral discretization using Fast Fourier Transforms. The inviscid fluxes ($\boldsymbol{E_c}$, $\boldsymbol{F_c}$ and in case finite differences are applied in the azimuthal direction also $\boldsymbol{G_c}$) are divided in an upwind flux and a downwind flux using van Leer's splitting [27]. Then, grid centered upwind differences (see Zhong [28]) with up to ninth-order accuracy are applied to evaluate the derivatives for these fluxes. These grid centered upwind differences are derived using a factor σ, which prescribes the degree of upwinding:

$$\left(\frac{\partial \phi}{\partial x}\right)^i_n = \sum_{k=i-N}^{i+N} c_k(\sigma)\phi^k_n - \sigma\overline{\Delta x}\left(\frac{\partial^{(2N)}\phi}{\partial x^{(2N)}}\right)^i_n + \cdots \tag{10}$$

Hereby $(\phi)^i_n$ denotes the flow variable at the grid point i and time step n, the c_k's are the stencil coefficients and $\overline{\Delta x}$ is the averaged grid spacing over the stencil interval. The parameter N determines the number of grid points in the stencil. For example the ninth-order upwind scheme is derived by setting $N = 5$ and $\sigma = -1500$. Note that for $\sigma = 0$ the upwind scheme reduces to a central difference scheme. All stencil coefficients are derived on a stretched grid.

Special attention is devoted to the boundary stencils next to the wall. Because high-order accurate boundary closures are typically unstable, the present code is adopting a method introduced by Zhong and Tatineni [29]. The fundamental idea is to stabilize the numerical scheme by using a stretched grid close to the wall (inflow: $\Delta y_w/\delta \sim 0.0067$, outflow: $\Delta y_w/\delta \sim 0.0038$). In particular, the following stretching function is applied:

$$y_j = \frac{\arcsin(-\eta \cos(\pi j/2n_y))}{\arcsin(\eta)} \tag{11}$$

This formula is a slight modification of Zhong's original formula, i.e., stretching is only applied at the wall boundary and not (as in Zhong and Tatineni [29]) at the wall and freestream boundary. For the present paper, the wall-normal stretching reduced the integration time step by only a factor of about 0.75 when compared with an equidistant grid. More details on the governing equations and the numerical scheme can also be found in Mayer [30]. Some notes on the accuracy of the numerical scheme for the wave equation can be found in Laible et al. [25].

D. Boundary Conditions

The inflow is separated into two regions: a subsonic region ($M < 1$) close to the wall and a supersonic region ($M > 1$). In the supersonic region, Dirichlet conditions for u, v, w, T, p and ρ are specified (e.g. obtained from the precursor calculation). For the subsonic region, a nonreflecting boundary condition is adopted as suggested by Poinsot and Lele [31] in order to avoid reflections of pressure waves traveling upstream in the subsonic region of the boundary layer. On the cone surface, the no-penetration ($v = 0$) and the no-slip ($u = 0$, $w = 0$) conditions are enforced. The wall is set to be adiabatic for the steady base flow and temperature fluctuations are assumed to vanish for the unsteady simulations because unstable disturbances at supersonic speed have a high disturbance frequency according to LST. The outflow boundary is treated by applying the condition $\partial\phi/\partial x = 0$ to all primitive variables. To avoid undesired reflections of waves a buffer domain technique is applied in addition, where finite amplitude disturbances are ramped to zero (see Meitz and Fasel [32]) between $x^* = 0.3$ m and $x^* = 0.327$ m. The streamwise extent of this buffer domain has been chosen large enough so that it does not have an upstream effect on the wave packet. Because for the simulations presented here, the freestream is located above the oblique shock, Dirichlet conditions (for u, v, w, T, p, ρ) can be enforced at this boundary. Note that if the high-order finite differences as previously described were used for the calculation of the shock, strong oscillations would be introduced into the computational domain. Therefore, before the simulation, the shock position is detected using the smoothness estimator IS_2^5 (given by Balsara and Shu [33]) on the pressure. Then, the order of accuracy of the wall-normal upwind difference stencils is decreased from ninth-order to first-order in the near shock region in order to avoid numerical oscillations. Because 1) the shock is multiple boundary-layer thicknesses away from the wall and 2) the gradients in the inviscid region are rather small, the higher truncation error of the first-order stencils have no significant effect of the overall accuracy of the scheme.

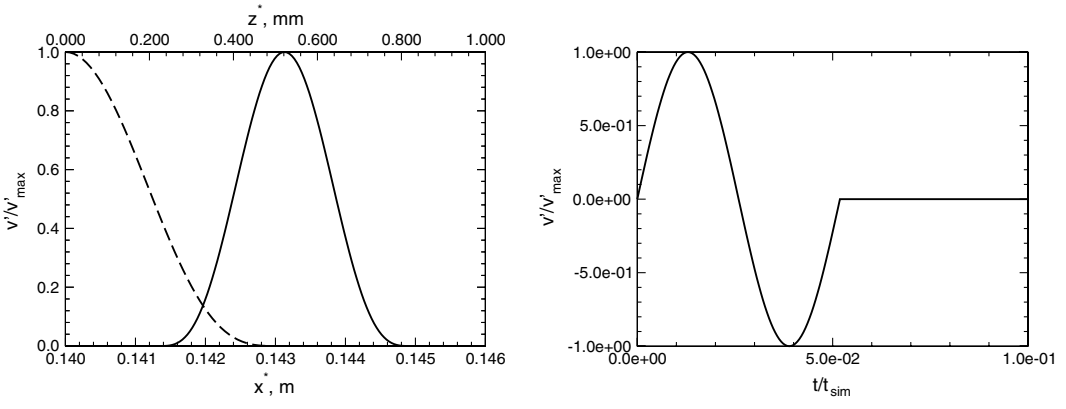

a) b)

Fig. 4 Wall-normal velocity at the wall: a) as a function of streamwise and azimuthal direction and b) as a function of time ($t_{sim} = 0.85$ ms). In (a), the dashed line (- -) represents the azimuthal distribution and the solid line (—) streamwise distribution of the wall-normal velocity.

E. Disturbance Generation

The flow was forced through a hole on the cone surface by pulsing the wall-normal velocity using a monopole with the streamwise and azimuthal distributions shown in Fig. 4a. The time signal of the pulse is plotted in Fig. 4b. The duration of the pulse is about 5% of the duration of the entire simulation. In dimensional form, this value corresponds to about $t_1 = 0.044$ ms while the entire simulation time is about 0.854 ms.

The forcing signal can be obtained from

$$v(x_h, y = 0, z_h, t) = \begin{cases} A\cos^3(\pi x_h)\cos^3(\pi z_h)\sin(-\omega t), & t < t_1 \\ 0, & t \geqslant t_1 \end{cases} \tag{12}$$

where x_h and z_h are defined as

$$x_h = \frac{x - 0.5(x_2 + x_1)}{x_2 - x_1} \quad \text{and} \quad z_h = \frac{z}{z_2 - z_1} \tag{13}$$

respectively. A denotes the forcing amplitude and ω the forcing frequency ($\omega^* \simeq 142$ rad/ms or $F = 2.0 \times 10^{-5}$). As demonstrated in Fig. 5, the monopole starts at $x_1^* = 0.1414$ m in streamwise direction and ends at $x_2^* = 0.1449$ m yielding a diameter of about 3.5 mm while in azimuthal direction the hole has a diameter of 1 mm.

Because the wall-normal velocity is excited, a nonzero mass flux is introduced. For the simulation with the large forcing amplitude in Sec. III.C, this mass flux (nondimensional) is rather small (in the order of 10^{-9}). Hence, only a minor difference in the nonlinear development of the wave packet between forcing the wall-normal velocity (v') and forcing the wall-normal mass flux ($\rho v'$) is expected here. Furthermore, for the linear transition regime in a periodically forced hypersonic boundary layer no difference was reported between both types of forcing in Wang and Zhong [34].

III. Results and Discussion

The objective of this study is to investigate the early nonlinear transition regime for a cone boundary layer at Mach 3.5. Our earlier investigations for flat-plate boundary layers [4,5] at Mach 2 and the experiments by Kosinov et al. [9] and Ermolaev et al. [35] for the same flow configuration showed that at least two physical mechanisms, oblique breakdown and asymmetric subharmonic resonance, play an important role for the transition process at supersonic speeds. So far, however, these transition mechanisms were only reported for numerical or experimental setups where oblique waves were periodically forced. Thus, it is unclear if these mechanisms or new mechanisms occur in a transition scenario, which involves a wide spectrum of disturbance and instability modes. To better understand a transition scenario initiated by a broadband disturbance spectrum, it is common [19–22] to study the spatial development of a wave packet in the boundary layer because in a wave packet a wide spectrum of disturbance waves is present. Therefore, in this work, the supersonic boundary layer is pulsed through a hole on the cone surface and as a consequence of this forcing, a wave packet is introduced into the flow. The spatial development of this wave packet is investigated in detail for both, the linear and the weakly nonlinear transition regime. Furthermore, using LST [23], subharmonic resonance triads and several new resonance triads are identified that might explain the weakly nonlinear disturbance development in the disturbance spectra of the wave packet obtained from the wall pressure.

A. Linear Regime

The linear regime is investigated by pulsing the flow through a hole (see Fig. 6a) with very small disturbance amplitudes [the amplitude A in Eq. (12) is 0.001% of the approach velocity U_∞] so that the wave packet remains within the linear regime throughout the entire computational domain. Note that the absolute value of the forcing amplitude for the simulations included in this paper (for both the linear and nonlinear regime) are a result of an extensive parameter study where several simulations with different forcing amplitudes were performed. These simulations are not shown here because they were only used for validating the computational setup and hence, do not provide additional insight into the flow physics.

The flow response to the forcing is illustrated in Fig. 6 by showing contours of the instantaneous wall pressure disturbances around the hole for different time instants on the unrolled cone surface. Note that throughout this paper all figures show either wall pressure or quantities that are obtained from wall pressure because this simplifies strongly the postprocessing of the large data amount from the simulations.

Towards the end of the duration of the pulse ($t^* = 0.043$ ms), an imprint of the developing wave packet on the wall pressure is clearly visible. The disturbance amplitudes of the wall pressure are in the order of 10^{-8} and for the streamwise velocity disturbance about one to two orders of magnitude higher. The flow structures that are visible in the wall pressure are strongly dependent on the contour levels chosen. In Fig. 6, the developing wave packet has a three-dimensional structure, which can be expected because at low and moderate supersonic Mach numbers oblique instability waves experience the highest streamwise amplification rates according to LST [36]. If the contour levels are decreased, different flow structures become apparent. In addition to the three-dimensional structures, which are composed of instability waves that grow in downstream direction, structures that have a rather two-dimensional (curved) wave front appear in Fig. 7. For Figs. 7a and 7b, these structures are still very close to the three-dimensional structures and become distinct farther downstream in Fig. 7c.

It seems that by pulsing the boundary layer three different wave packets are generated. The first two wave packets have a rather two-dimensional wave front and are denoted by *1* and *2* in Fig. 7c. They travel at a higher group velocity than the third wave packet denoted by *3*, which contains the instability waves. Wave packet 1 is generated during the interval of the pulse when fluid is blown into the

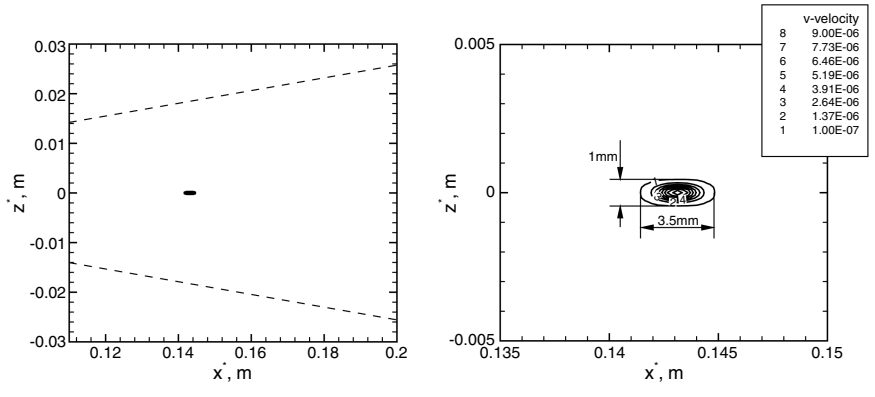

Fig. 5 Illustration of the disturbance generation for $t^* = 0.011$ ms: a) streamwise and azimuthal position of the hole on the unrolled cone surface [dashed line (- -) indicates boundaries of the computational domain] and b) contours of wall-normal velocity.

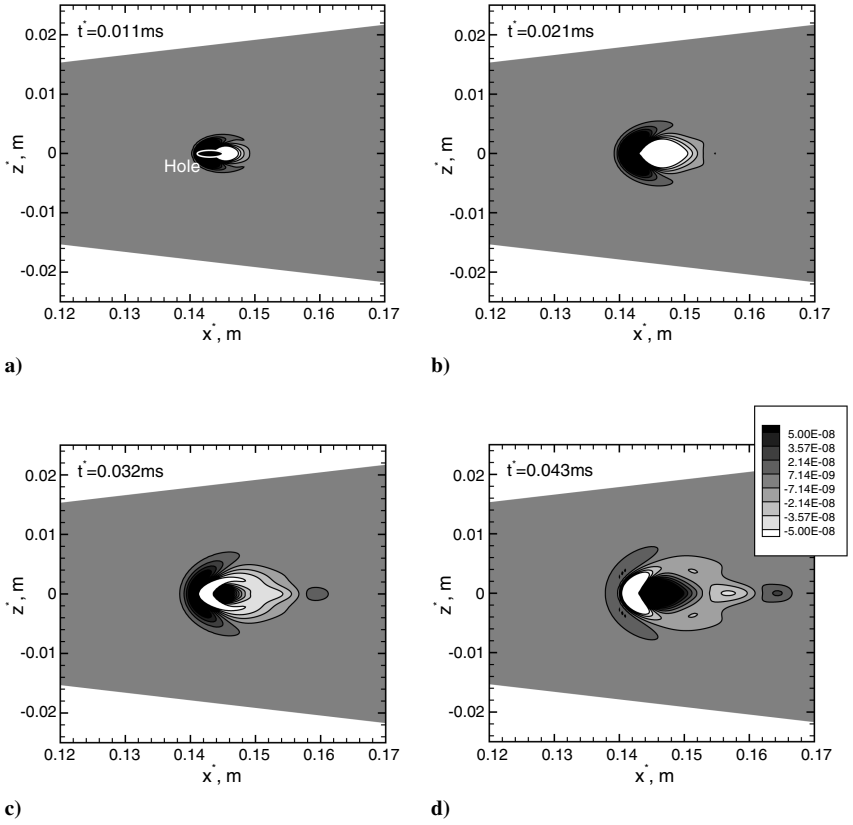

Fig. 6 Flow response in wall pressure on the unrolled cone surface to the forcing described in Sec. II.E at different time instants. The physical time increases from (a)–(d).

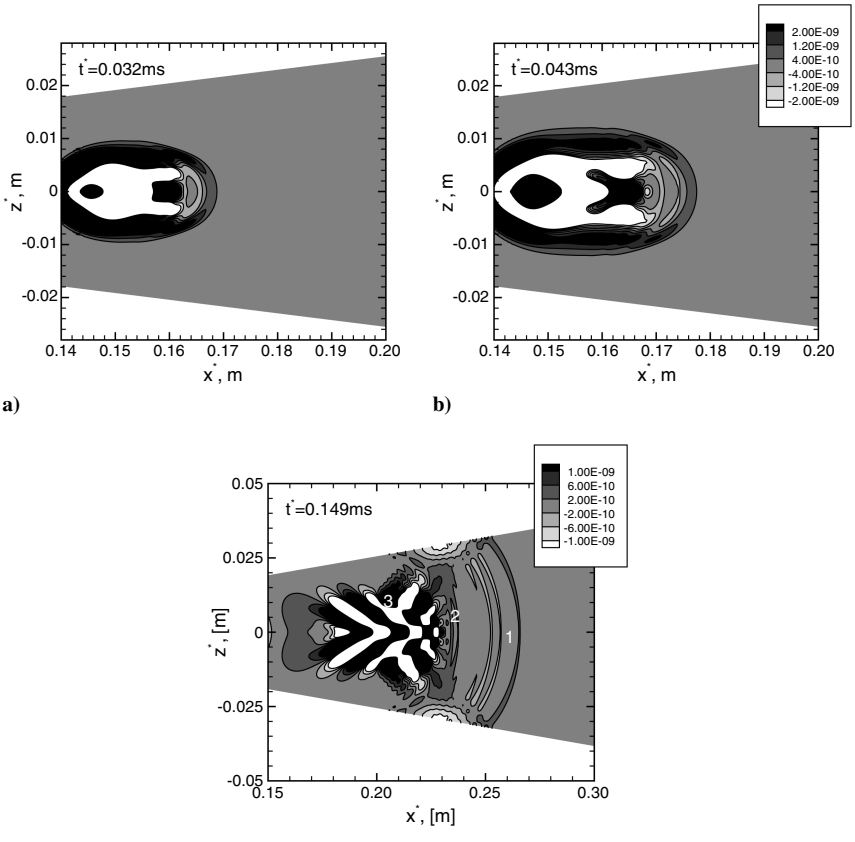

Fig. 7 Excitation of three different wave packets illustrated by contours of wall pressure (on unrolled cone surface). The contour levels in this figure are about one order of magnitude smaller than in Fig. 6. The physical time increases from (a)–(c).

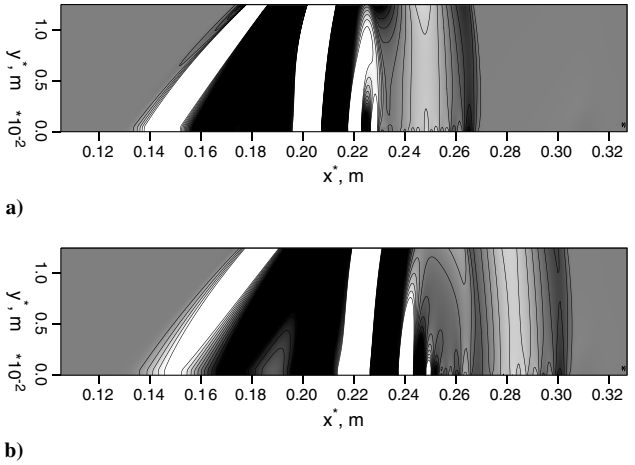

Fig. 8 Contours of pressure disturbance at the centerline for a) $t^* = 0.149$ ms and b) $t^* = 0.192$ ms. Contour levels (between -1.0×10^{-10} and 1.0×10^{-10}) are chosen such that the contrast is increased in order to highlight the fast traveling wave packets (1 and 2) in the front.

boundary layer while wave packet 2 evolves when fluid is sucked from the boundary layer (see also Fig. 4b). Both of these wave packets are damped in streamwise direction and vanish farther downstream. To provide an evidence whether wave packets 1 and 2 contain fast acoustic disturbances or damped discrete modes that are commonly referred to as fast modes [37], Fig. 8 shows the contours of the pressure disturbance in a plane normal to the azimuthal direction at the centerline. Structures are visible that have a larger amplitude close to the wall. This might be an indication that discrete modes (boundary-layer modes) are present. To determine the true nature of these fast traveling wave packets would, however, require a detailed analysis using multimode decomposition according to Tumin et al. [38,39]. Such a study is beyond the scope of this paper because the nature of these wave packets might not be of great importance for the transition process, which is initiated by wave packet 3.

Figure 7c also emphasizes that the choice of the domain width (one third of the cone) is large enough for wave packet 3 while both faster traveling wave packets reach the azimuthal boundaries. Note that disturbances in both faster traveling wave packets are significantly lower in amplitude. The independence of the solution on the azimuthal domain width for wave packet 3 was further confirmed by a simulation with one half of the cone as azimuthal domain. In the following sections, the focus is on wave packet 3 because the amplitudes of its disturbance spectrum grow strongly in streamwise direction and therefore, this wave packet is mainly responsible for the transition process. The streamwise development of the disturbance spectrum obtained from a Fourier transformation of the wall pressure disturbance using 100 modes in time and azimuthal direction is displayed in Fig. 9. The period of the smallest frequency, which has the value of $f^* = 1.171$ kHz, corresponds to the simulation time t_{sim} (0.85 ms). Note, as discussed in Sec. II.A, the highest frequency that can be accurately resolved by the streamwise resolution of the simulation has a value of $F = 10^{-4}$, which is above 110 kHz. Hence, all instability waves that experience strong streamwise growth for a conical boundary layer at Mach 3.5 are included in the present simulations.

The disturbance spectra in Fig. 9 are typical for a supersonic boundary layer. The maximum has a finite azimuthal mode number k_c unequal to zero. Thus, as already known from LST [36], oblique disturbances have the strongest streamwise amplification rates. With increasing downstream location, the peak amplitude in Fig. 9 shifts to higher azimuthal mode numbers. At the end of the computational domain, this peak is located close to frequency $f^* = 23.415$ kHz and to azimuthal mode number $k_c = 21$.

In the following two figures, results from the DNS with the low forcing amplitude are compared with predictions from LST in order to further validate the computational setup. The first figure (Fig. 10) shows the complex wave number $\alpha = \alpha_r + i\alpha_i$, which is calculated from the DNS data using the wall pressure disturbance [40,41] and the following relation:

$$\alpha_i = -\frac{\mathrm{d}}{\mathrm{d}x}[\ell_n(A(x))], \qquad \alpha_r = \frac{\mathrm{d}}{\mathrm{d}x}[\theta(x)] \tag{14}$$

where A represents the amplitude and θ the phase of the disturbance of interest. Because a wave packet contains a wide range of frequencies and azimuthal mode numbers, the complex wave number is plotted as a function of streamwise direction, frequency and azimuthal mode number in Fig. 10. To solve the eigenvalue problem posed by LST [36,42] for a compressible boundary layer, the linear stability solvers from Mack [11,43] and Tumin [38] are employed. In Fig. 10, symbols represent results from Tumin's solver [38] while solid lines indicate results from Mack's solver. Note that both solvers do not account for curvature or divergence effects resulting from the cone geometry. Because the computational domain is far downstream of the nose tip of the cone and the curvature parameter χ_δ as defined by Malik and Spall [44] is below 5% at the inflow, curvature effects are assumed to be very weak for the present work (see also Laible et al. [24] Fig. 10). Hence, it is justified to compare the results of both LST solvers to the DNS data set.

In general, the streamwise wave number α_r is less sensitive to the criterion used for its computation or nonparallel effects resulting from the growth of the boundary layer. Thus, the agreement between DNS and LST (Tumin's solver) is nearly perfect in Figs. 10a, 10c, and 10e. The difference between Mack's solver and Tumin's solver is only due to the different mean flow profiles used for the stability analysis. For the linear stability analysis using Mack's solver, self-similar compressible boundary-layer profiles are applied whereas for

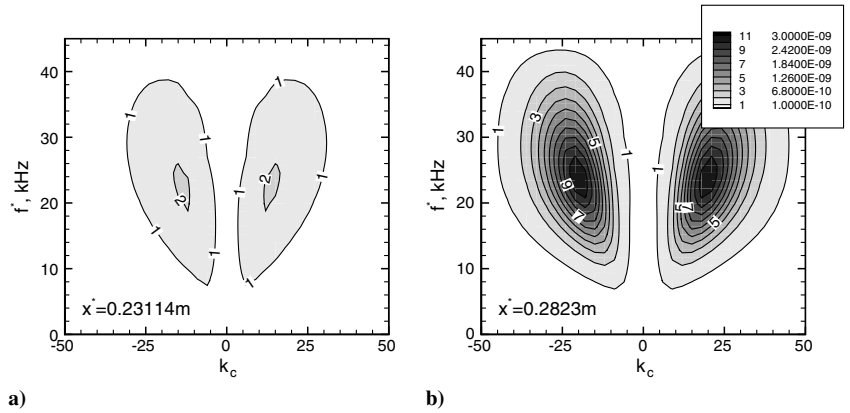

Fig. 9 Streamwise development of the Fourier amplitude obtained from wall pressure in the frequency–azimuthal wave number plane, with f^* as dimensional frequency and k_c as azimuthal wave number. The smallest frequency has a period based on the simulation time $T = t_{\text{sim}}$ and has the value of about $f^* = 1.171$ kHz.

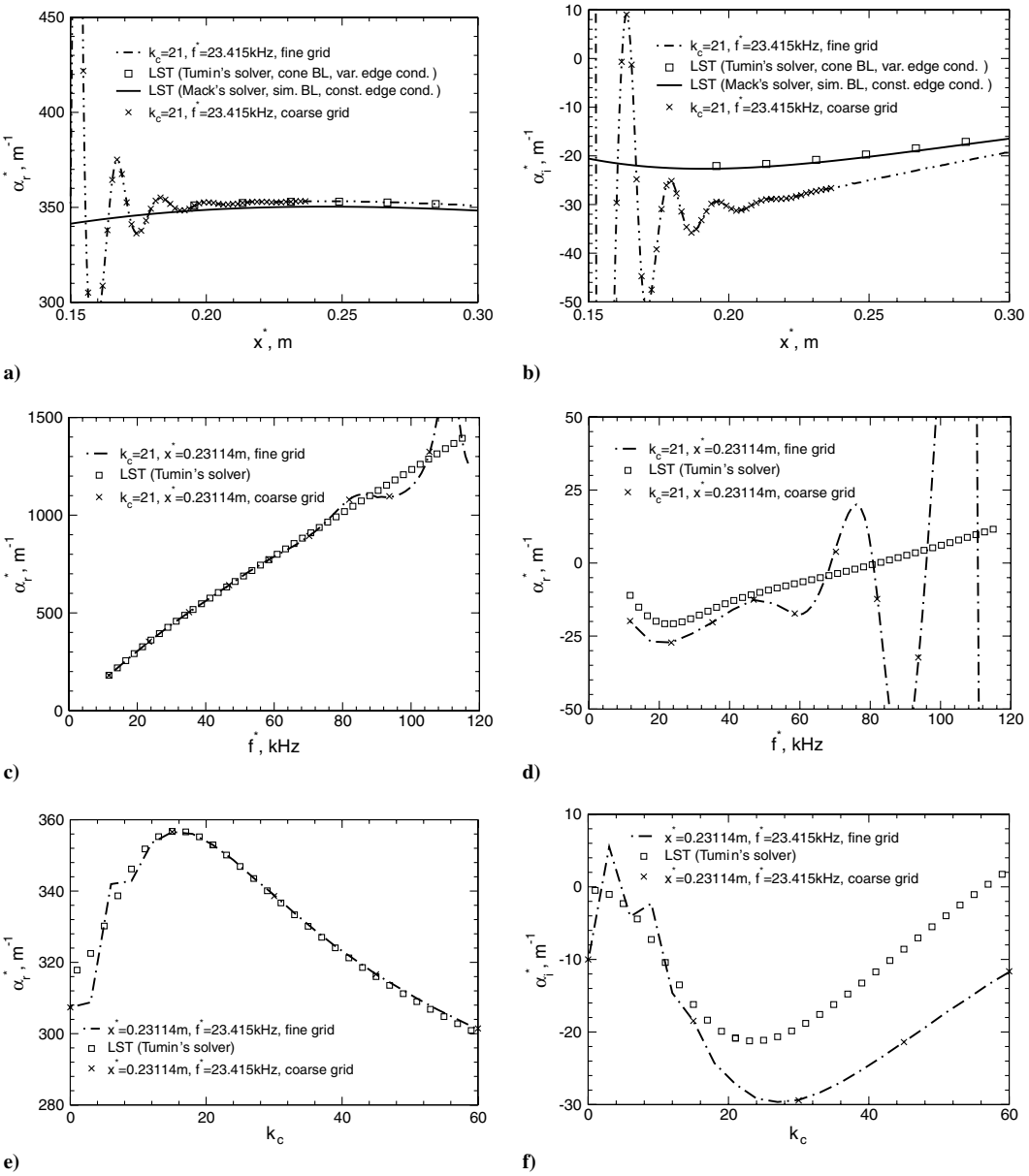

Fig. 10 Comparison of complex wave number α vs a–b) streamwise direction, c–d) frequency, and e–f) azimuthal wave number, obtained from wall pressure to theoretical predictions from LST and a simulation with a coarser grid.

Tumin's solver, the mean flow was obtained by numerically solving the Navier–Stokes equations with our DNS code.

For disturbances with weak streamwise amplification (see Figs. 10b, 10d, and 10f), or close to the forcing hole, the streamwise wave number α_r from the DNS is modulated by the fast traveling wave packets generated by the forcing. This modulation is even more pronounced for α_i in Figs. 10b, 10d, and 10f. α_i is somewhat underpredicted by LST when compared with the DNS. This behavior has also been reported in earlier investigations [6,8,24,40,41]. For compressible boundary layers, nonparallel effects are more dominant than for incompressible flow and thus, the parallel flow assumptions in LST may introduce a significant error. Note that this error depends on α_i because Ma and Zhong [40] and Sivasubramanian et al. [45] observe a better agreement between both methods close to the maximal streamwise amplification rate for a hypersonic cone boundary layer.

The wall-normal amplitude and phase distribution from the DNS for selected flow quantities at frequency $f^* = 23.415$ kHz, azimuthal mode number $k_c = 21$ and streamwise position $x^* = 0.23114$ m are plotted in Fig. 11. Also included are the results from LST. The amplitude distributions from both, LST and DNS, are normalized by their respective maximum value within the boundary layer. The excellent agreement in Figs. 10a, 10c, 10e, and 11 between LST and DNS indicates that our simulations capture the linear disturbance development accurately. Even the simulation with the coarser wall-normal grid yields the same results.

The actual time signal of the wave packet, before it was Fourier transformed in time and azimuthal direction for the preceding discussion, is plotted for the wall pressure on the centerline of the wave packet in Fig. 12 for different streamwise positions. Plotting the wave packet in this way is very convenient for experimentalists because they only need to measure the time signal of one disturbance quantity, here the wall pressure, at a few streamwise positions on the centerline. Furthermore, this figure provides an impression of how the center region develops in downstream direction. Clearly, with increasing downstream location the wave packet spreads. Initially, at $x^* = 0.199$ m, the wave packet consists of about two wave lengths while farther downstream about three wave lengths are visible. The envelopes of these time signals, computed using Fourier transformations according to Gaster and Grant [19], exhibit one dominant peak. At $x^* = 0.199$ m, this peak is close to the tail of the wave packet while farther downstream, it shifts towards the center. The propagation speeds of the front and the tail of the wave packet are indicated by the dotted lines in Fig. 12. The velocity of the wave

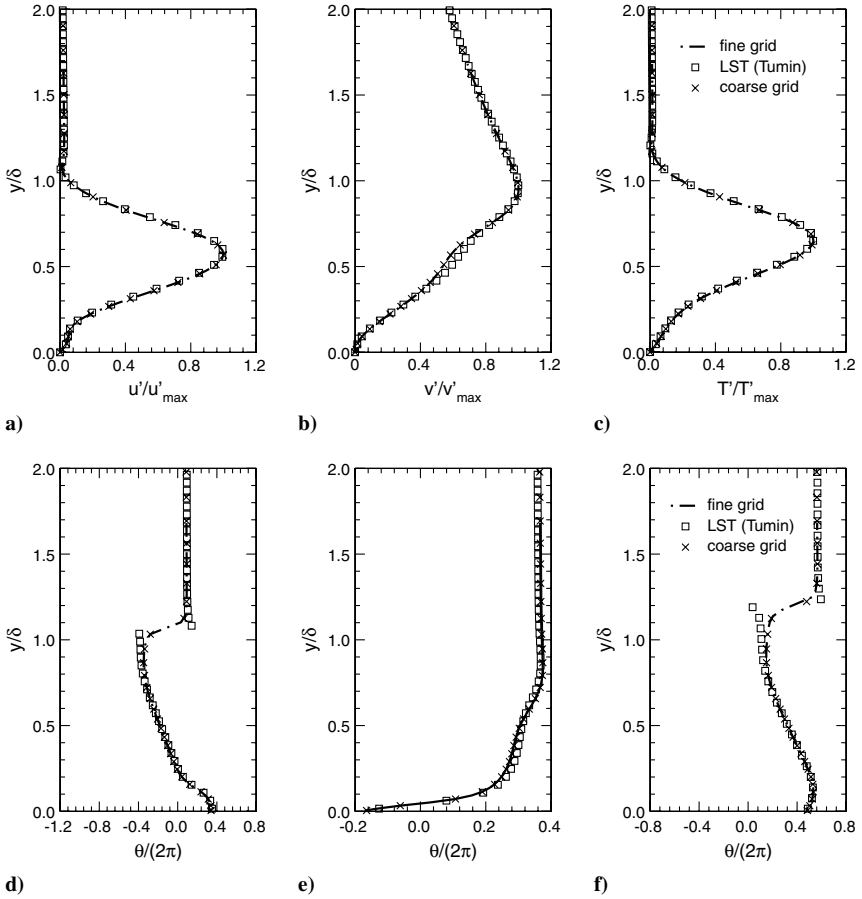

Fig. 11 Comparison of a–c) wall-normal amplitude and d–f) phase distributions to theoretical predictions from LST and a simulation with a coarser grid for frequency $f^* = 23.415$ kHz, azimuthal mode number $k_c = 21$ and streamwise position $x^* = 0.23114$ m. All LST results are computed using Tumin's solver [38] with mean flow profiles from the DNS.

packet front is about 550 m/s while the velocity of the tail is slower ($\simeq$ 420 m/s).

Contours of constant amplitude (envelopes) as a function of the azimuthal angle φ are given in Fig. 13. This figure demonstrates the overall development and therefore azimuthal extent of the wave packet. Initially, the wave packet has the form of a "butterfly" with the maximal amplitude values on the centerline and two smaller side peaks or "tongues" at about $\varphi \simeq \pm 0.2$ in the front part of the packet. Farther downstream, additional tongues at higher angles develop until in the last plot (Fig. 13f) a total number of seven tongues appear. The maximal disturbance amplitude shifts from the centerline to the two side peaks at about $x^* = 0.256$ m.

When transformed into the x-z plane, as shown in Fig. 14 (right) for different time instants on the unrolled cone surface, the wave packet has the shape of a hand. Again, initially the maximal disturbance amplitude is located on the centerline $z^* = 0.0$ m and two smaller side peaks, which have the shape of fingers, are present. While the wave packet travels downstream, additional fingers arise and the maximal amplitude shifts from the centerline to the side peaks. The original three-dimensional signal that was used for the calculation of the envelope in Fig. 14 (right) is illustrated in Fig. 14 (left). One contour line from the envelope plots is also shown in order to roughly define the boundary of the wave packet. The packet structure is entirely three-dimensional because the three-dimensionality results from strongly amplified oblique instability waves. Moreover, the wave packet spreads rapidly in streamwise and azimuthal direction.

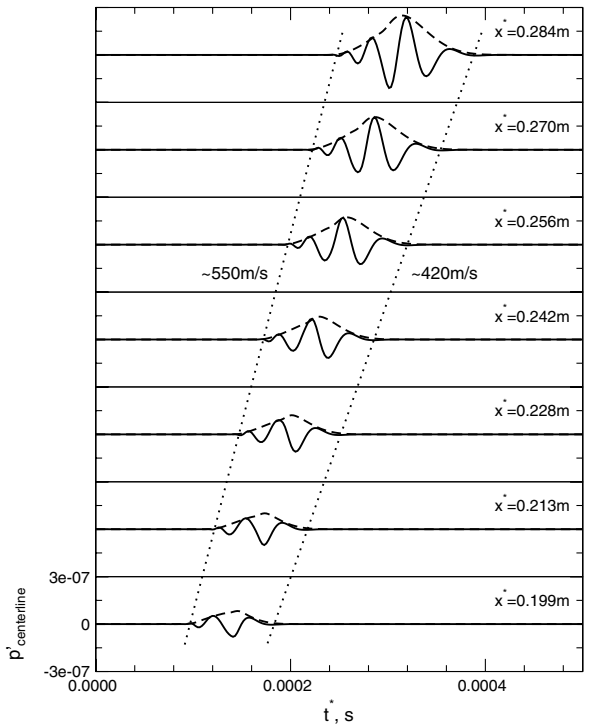

Fig. 12 Temporal evolution of wall pressure disturbance amplitude and its envelope for different streamwise positions along the centerline of the wave packet. Dotted lines (. . .) are an estimate for propagation speed of the front (∼550 m/s) and the tail (∼420 m/s) of the wave packet. Solid lines (—) represent the time signal and dashed lines (- -) its envelope.

B. Identification of Possible Resonance Triads Using Linear Theory

Before discussing the nonlinear transition regime initiated by a high-amplitude wave packet, possible resonance triads according to Craik [23] are identified for the flow conditions discussed in this

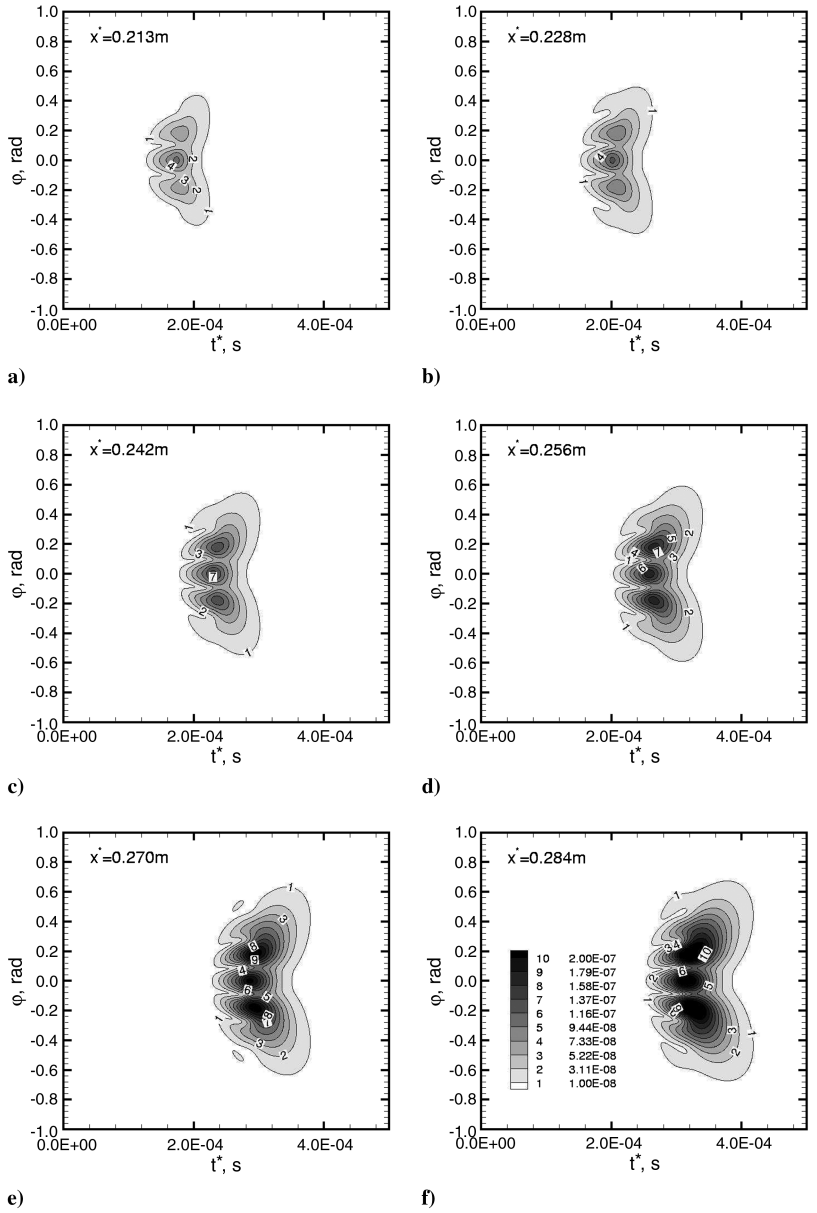

Fig. 13 Temporal evolution of contours of constant amplitudes (envelopes) from wall pressure for different azimuthal angles φ at several streamwise positions. All plots use the same contour levels.

paper. As shown by Kosinov and coworkers [9,35], who investigated asymmetric subharmonic resonance in a wave train at Mach 2, resonance triads are important transition mechanisms in supersonic boundary layers. Craik [46] even further states for incompressible boundary layers that for "all nonresonant cases, the forced quadratic disturbance remains relatively small" when compared with the resonant cases. A theoretical study of resonance triads for the present flow configuration, therefore, allows to predict possible weakly nonlinear wave interactions and might help to understand the weakly nonlinear development of a wave packet.

Because a wave packet consists of a wide range of instability waves, also a wide range of nonlinear wave interactions are possible. To simplify the following study, only resonance triads for instability waves with azimuthal mode number $k_c = 21$ and frequency $f^* = 23.415$ kHz are determined. As discussed in Sec. III.A, instability waves with this azimuthal mode number and frequency experience strong streamwise growth and thus, reach the highest amplitudes at the outflow for our setup.

Using the stability solver of Mack [43], linear stability data for a large number of frequencies and azimuthal mode numbers were generated. These data were used as input for a software tool, which calculates the azimuthal mode number k_c for possible resonance triads within the limits of the data set according to the resonance conditions as introduced by Craik [23]:

$$\omega^1 = \omega^2 + \omega^3, \qquad \alpha_r^1 = \alpha_r^2 + \alpha_r^3, \qquad \beta^1 = \beta^2 + \beta^3 \tag{15}$$

with ω as angular frequency, β as azimuthal wave number and α_r as streamwise wave number. For a cone, the resonance condition for the azimuthal wave number β can be recast to

$$k_c^1 = k_c^2 + k_c^3 \tag{16}$$

To locate any resonance triad in the data set, the frequency and the azimuthal mode number k_c for the primary wave (here $f^* = 23.415$ kHz, $k_c = 21$) and the frequency of one secondary wave have to be specified. In the succeeding paragraphs, the primary (fundamental) wave of a triad is always denoted by a superscript of 1 and the secondary waves are always denoted by the superscripts 2 and 3.

Before determining possible resonance triads using the previously mentioned software tool, the procedure to locate a subharmonic resonance triad is explained. For more detail see also Mayer and Fasel [5]. Figure 15 shows the streamwise wave number α_r as a

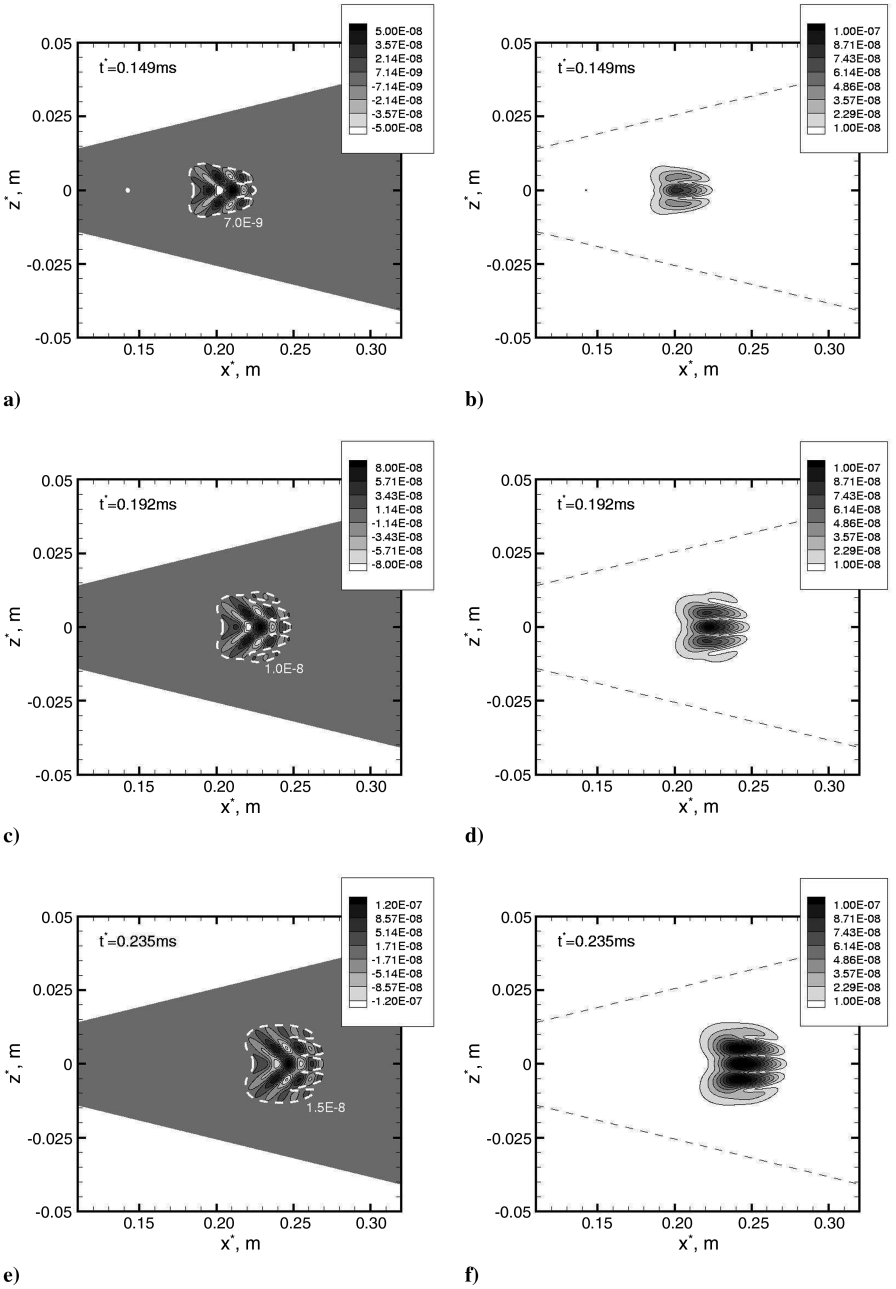

Fig. 14 Spatial evolution of wall pressure revealing the wave structure (left) and the envelopes (right) on the unrolled cone surface for different time instances.

function of the azimuthal mode number k_c for the fundamental and subharmonic frequency at $R_x = 1600$ (0.24 m). To satisfy the resonance condition for the azimuthal mode number ($k_c^1 = k_c^2 + k_c^3$), both subharmonic waves of the triad need to have a difference in their azimuthal mode number that has the value of the azimuthal mode number of the primary, fundamental wave, which is denoted by a vertical line in Fig. 15b. Because we are looking for a triad with $k_c^1 = 21$ as the azimuthal mode number for the primary wave (superscript 1), the azimuthal distribution of α_r for the subharmonic frequency in Fig. 15b (- -) is mirrored and shifted by $\Delta k_c = 21$ in order to generate a second graph (—). The labeling on the bottom of Fig. 15b (and also 15c and 15d) refers to the first graph with subharmonic frequency (- -) while the labeling on the top belongs to the second graph (—). Each graph contains one secondary wave of a resonance triad as illustrated in the following. To satisfy the resonance condition for the streamwise wave number ($\alpha_r^1 = \alpha_r^2 + \alpha_r^3$) both graphs of the streamwise wave number for the subharmonic frequency in Fig. 15c are added (-.-). The resulting graph exhibits the value of the streamwise wave number of the fundamental, primary wave with $k_c^1 = 21$ at four points indicated by black dots in Fig. 15d (the points for negative k_c are not shown here). One subharmonic resonance triad is highlighted by the vertical line in Fig. 15d and the three arrows represent all three waves included in the triad. The azimuthal mode number at this position is about 36 (bottom label). Hence, the black dot at 36 in Fig. 15d suggests the existence of a resonance triad, which is composed of one primary wave with fundamental frequency of $f^* = 23.415$ kHz and azimuthal mode number of $k_c^1 = 21$ and two subharmonic waves with $k_c^2 \sim -15$ (top label) and $k_c^3 \sim 36$ (bottom label).

Figure 16 summarizes the results of our search for subharmonic resonance triads using the previously mentioned tool and LST data for the fundamental frequency $f^* = 23.415$ kHz. The azimuthal mode numbers $k_c^{2,3}$ of both subharmonic waves included in the triad as a function of the azimuthal mode number of the fundamental wave k_c^1 is shown in Fig. 16a. Because in this work the focus is on $k_c^1 = 21$, Fig. 16b illustrates the streamwise development of the azimuthal mode number for both subharmonic waves at exactly $k_c^1 = 21$. Both figures show three subharmonic resonance triads. For all three triads

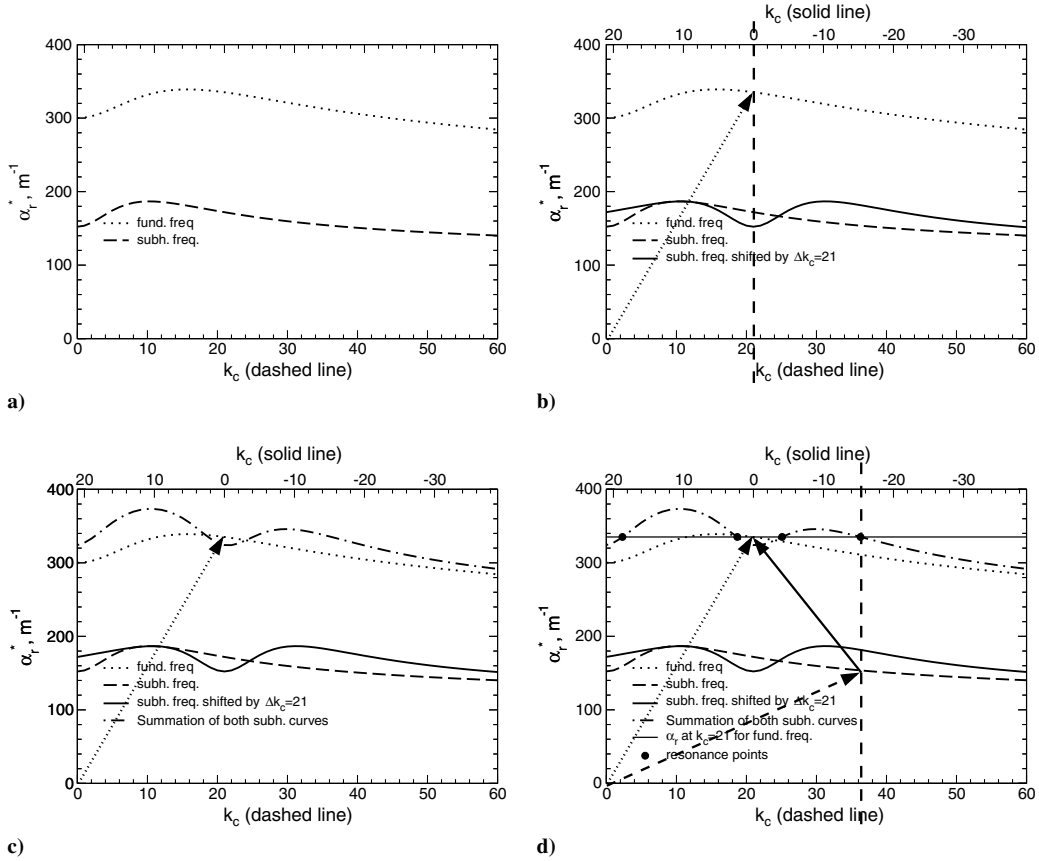

Fig. 15 Illustration of the procedure used to determine a particular asymmetric, subharmonic resonance triad using LST results at $R_x = 1600$ (0.24 m): a) azimuthal distribution of streamwise wave number for the fundamental and subharmonic frequency; b) value of azimuthal mode number for the fundamental wave set to $k_c = 21$ [to fulfill the resonance condition for the azimuthal mode number ($k_c^1 = k_c^2 + k_c^3$), the curve for the azimuthal distribution of the streamwise wave number for the subharmonic frequency is shifted by $\Delta k_c = 21$]; c) both curves for the subharmonic frequency added; and d) determination of the resonance triads [note that the arrows denote the different components (waves) of one triad].

in Fig. 16b, the azimuthal mode number of the subharmonic waves is changing in streamwise direction suggesting that at every streamwise position a different pair of subharmonic waves is necessary to close the triad. For a particular range of the local Reynolds number, this change is, however, very weak. Hence, the first subharmonic triad (no symbols) might be strong from $R_x = 1200$ to $R_x = 1400$ while the other two subharmonic resonance triads ($\times$ and $\square$) might be dominant from $R_x = 1600$ to $R_x = 1800$. Close to the end of the computational domain at about $R_x = 1960$, two subharmonic resonance triads become detuned ($\times$ and $\square$) because the resonance conditions are not satisfied anymore.

At this point it is not possible to determine the most dominant triad in Fig. 16. Several factors such as, the linear amplification of all three waves included in the triad, the phase relation between all three waves (Mayer and Fasel [5]) and the streamwise change in the azimuthal mode number for the subharmonic waves included in the triads, influence the strength of the resonance interaction. The impact of these factors on the resonance interaction have to be studied in greater detail. For this paper, we have instead concentrated on identifying resonance triads with secondary waves over a broad range of frequencies and not simply for the first subharmonic frequency of the primary mode. More general triads of this type have

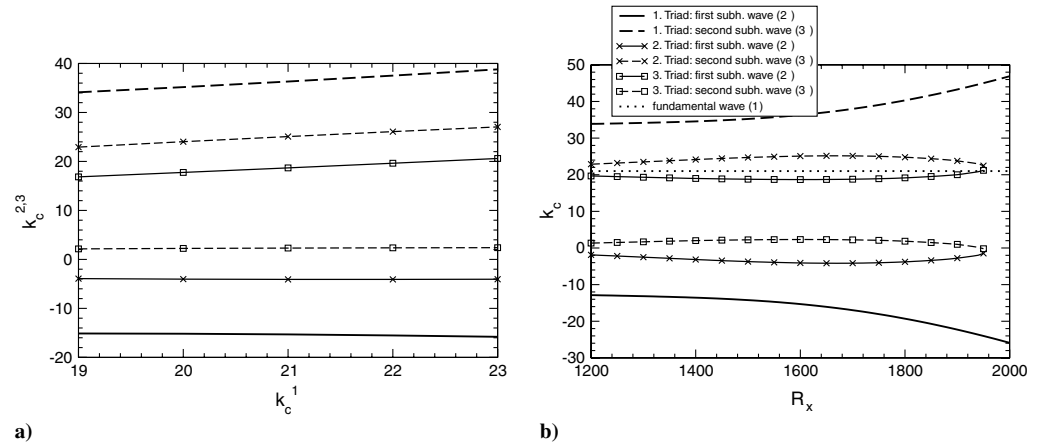

Fig. 16 Possible subharmonic resonance triads for $k_c^1 = 21$ obtained from LST data: a) dependency of azimuthal mode number of the waves with the subharmonic frequency on the azimuthal mode number of the fundamental wave at $R_x = 1600$ (0.24 m) and b) streamwise development of the azimuthal mode number for both subharmonic waves.

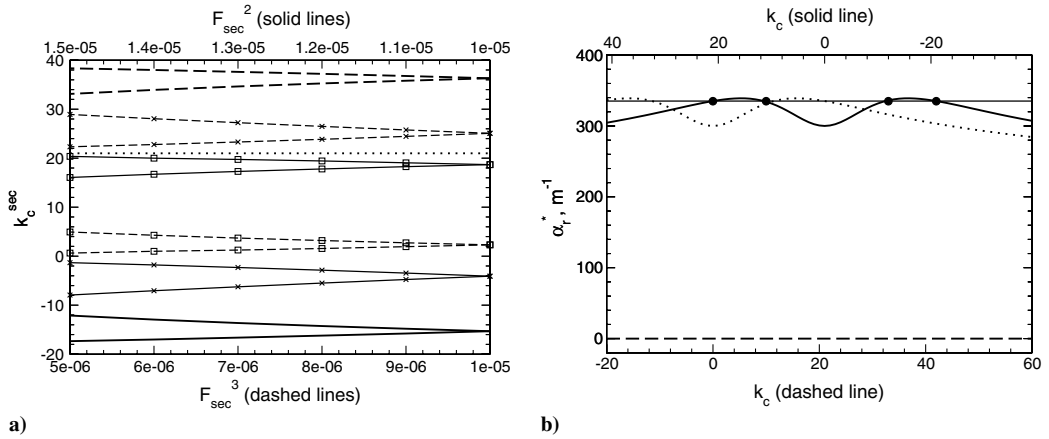

Fig. 17 Possible resonance triads where the secondary waves have a frequency unequal to a subharmonic frequency: a) dependency of azimuthal mode number of the secondary waves included in the resonance triads on their frequency for $R_x = 1600$ (0.24 m) and $k_c^1 = 21$ (different symbols indicate different resonance triads and the line style distinguishes between both secondary waves that close the triad) and b) illustration of how Fig. 15d would look like when one secondary wave reaches zero disturbance frequency.

never been reported for a supersonic boundary layer. Figure 17 summarizes our efforts in this regard for the streamwise position $R_x = 1600$ (0.24 m) and $k_c^1 = 21$. The dependency of the azimuthal mode number of the secondary waves included in the triad on their frequency is demonstrated in Fig. 17a. The two line styles distinguish between the different secondary waves, where a solid line indicates the first secondary wave (superscript 2) and a dashed line the second secondary wave (superscript 3). The different symbols represent different resonance triads. If the frequency of both secondary waves deviates from the subharmonic frequency (the frequency for one secondary wave has to increase and for the other to decrease according to $\omega^1 = \omega^2 + \omega^3$) additional resonance triads appear. Every subharmonic resonance triad splits into two new triads (in Fig. 17a at $F_{\text{sec}} = 10^{-5}$). The limit for one secondary frequency converging to zero is depicted in Fig. 17b. The azimuthal distribution of the streamwise wave number tends to zero (- -) for zero disturbance frequency (first secondary wave, superscript 2) whereas the azimuthal distribution of the streamwise wave number including the second secondary wave (superscript 3) tends to the distribution of the fundamental frequency (—) shifted by $k_c = 21$.

The resulting resonance triads for one secondary frequency $F \rightarrow 0.0$ are summarized in Fig. 18. Three main cases can be observed, where the first case (Fig. 18a) represents the interaction of the primary instability wave with the mean flow, the second (Fig. 18b), a fundamental resonance of the oblique primary wave with an oblique secondary wave with the same frequency but different azimuthal mode number k_c and the third, oblique breakdown. All these "triads" have a counterpart, mirrored at $k_c = 0$, with instability waves traveling at opposite wave angles except for oblique breakdown (third case) where the counterpart is the same as the original mechanism. Note that the triad at $k_c \sim 33$ in Fig. 18 is of the same nature as the second case (Fig. 18b) but with a different azimuthal mode number and therefore, is not listed separately as a fourth limiting case.

The outcome of this study can be used to address the question whether oblique breakdown or any other resonance triad is a dominant mechanism in the transition process of a boundary layer at supersonic Mach numbers. The three factors previously mentioned that influence the strength of a resonance interaction suggest that oblique breakdown is the strongest nonlinear mechanism because both oblique instability waves, initiating oblique breakdown, experience the strongest amplitude growth according to linear theory, and the wave-vortex triad is always synchronized in downstream direction. However, the effect of the phase relation between these modes still needs to be investigated in detail.

All triads found in this section are summarized in Fig. 19, which shows the disturbance spectrum at $R_x = 1600$ (0.24 m) for the wave packet discussed in Sec. III.A. The white circle at $k_c = 21$ denotes the primary wave with $f^* = 23.415$ kHz while the other circles denote the subharmonic resonance triads. Filled circles indicate subharmonic waves that mainly experience linear growth whereas unfilled circles represent subharmonic waves that are expected to grow due to the resonance. This distinction between the subharmonic waves is based on their amplitude level in the frequency–azimuthal wave number plane in Fig. 19. Lines demonstrate the frequency and azimuthal wave number for the new resonance triads with secondary waves that do not have a subharmonic frequency. The dashed lines predict positions where strong resonance growth might appear.

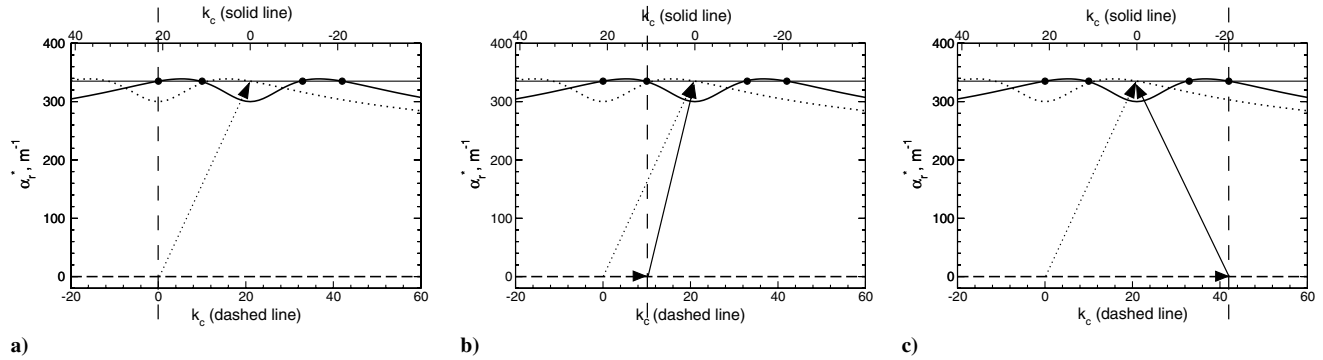

Fig. 18 Illustration of possible resonance triads with one secondary frequency reaching zero ($F \rightarrow 0.0$) using wave vectors ($R_x = 1600$ (0.24 m) and $k_c^1 = 21$): a) interaction between the primary wave and the mean flow, b) fundamental resonance between the oblique primary wave and an oblique secondary wave with the same frequency but different azimuthal mode number k_c, and c) oblique breakdown (interaction between the oblique primary wave and an oblique secondary wave with the same frequency and the opposite azimuthal mode number $k_c^2 = -k_c^1$ than the primary wave).

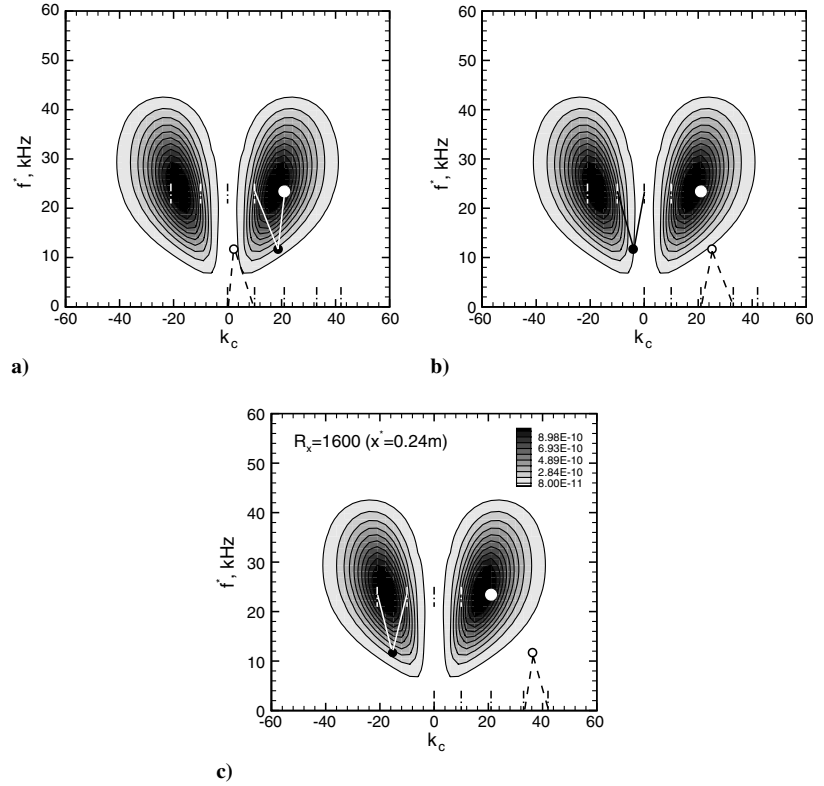

Fig. 19 Disturbance spectrum in the frequency–azimuthal mode number plane for the wave packet of Sec. III.A obtained from wall pressure at the streamwise position $R_x = 1600$ (0.24 m). Circles indicate the position of subharmonic resonance triads identified in Fig. 16 and lines demonstrate their limiting behavior for one frequency converging to zero (Fig. 17). The white circle at $k_c = 21$ denotes the primary wave while the subharmonic waves that are expected to experience resonance growth are denoted by the circles that are not filled. Figures (a)–(c) illustrate different resonance triads. The dashed lines predict positions where strong resonance growth might appear.

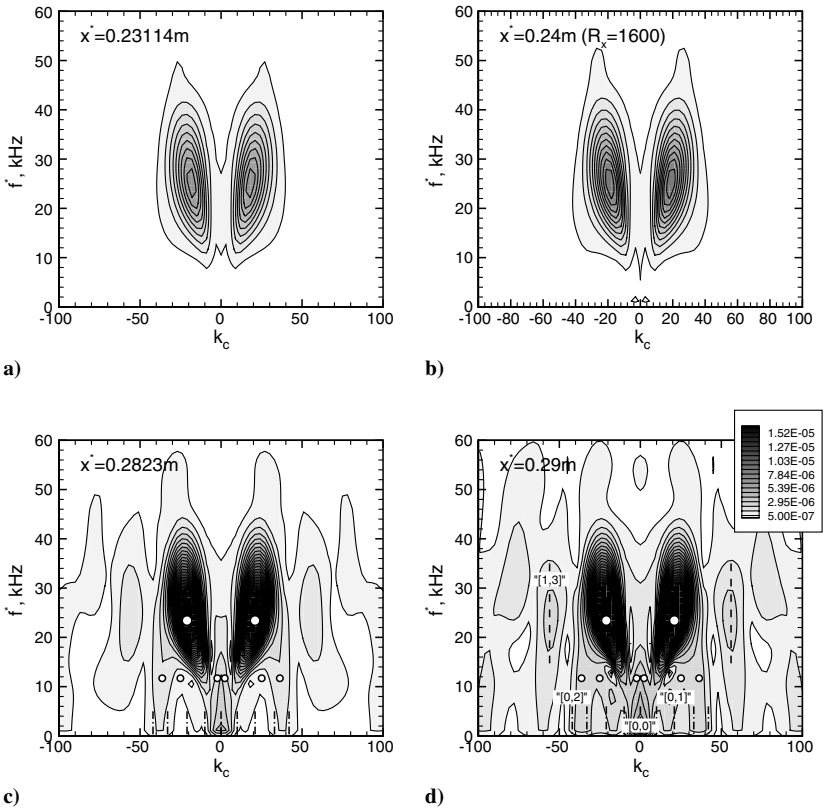

Fig. 20 Disturbance spectrum in the frequency–azimuthal mode number plane for the simulation with the high forcing amplitude (6% of the approach velocity U_∞) obtained from wall pressure at different streamwise positions. Circles indicate the position of the subharmonic resonance triads identified in Sec. III.B. The vertical dashed-dotted lines close to the abscissa represent the azimuthal mode numbers of the cases with $F \rightarrow 0.0$ for one of the secondary waves in Sec. III.B.

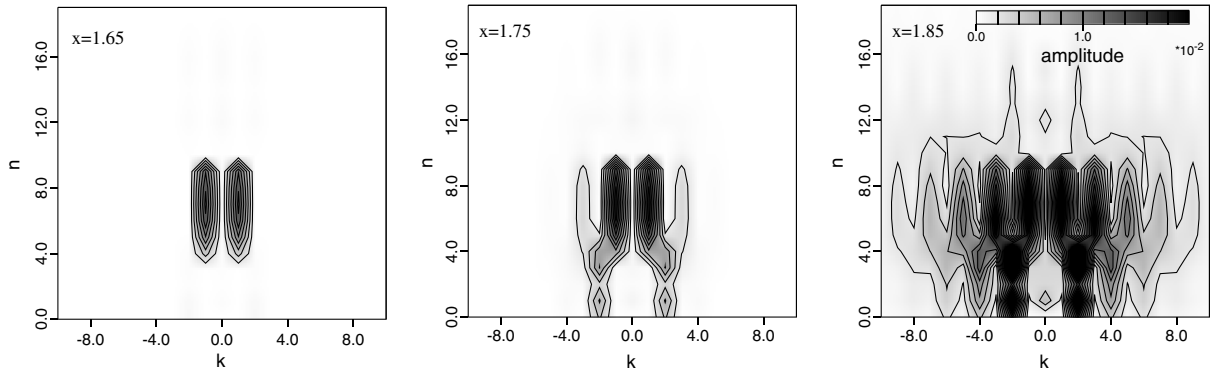

Fig. 21 Streamwise development of disturbance spectra in the frequency–azimuthal mode number plane from Laible et al. [25] These spectra are obtained from a simulation (case B) that models natural transition for the same flow configuration as in the present work. Only oblique modes, as typical for oblique breakdown, are introduced into the computational domain by prescribing their linear eigenfunctions and a random phase at the inflow. Note that the computational domain is farther downstream than in the present work and only 1/32 of the cone is simulated. n and k denote multiples of the fundamental frequency and fundamental azimuthal mode number ($k_c = 32$).

C. Weakly Nonlinear Regime

The study of resonance triads in the previous section provides an idea of the frequencies and azimuthal mode numbers where possible resonance growth might occur for the investigated wave packet (wave packet 3 in Sec. III.A). Because a wave packet is composed of a large number of waves, the focus on the resonance interactions of one primary wave, as applied in this study, is a strong simplification of the real weakly nonlinear development. Moreover, it is unclear if the new resonance triads, where the secondary waves have no subharmonic frequencies, indeed constitute possible transition mechanisms. The results presented in this section, however, suggest that our simplified study of resonance triads can explain the weakly nonlinear regime for a wave packet. A new simulation was performed with a higher forcing amplitude [the amplitude A in Eq. (12) is 6% of the approach velocity U_∞]. The initial spatial development of the wave packet is still linear for this simulation. Farther downstream, the flow field is altered by nonlinear wave interactions.

The streamwise development of the disturbance spectrum in the frequency–azimuthal wave number plane for the simulation with the higher forcing amplitude is given in Fig. 20. In this figure, circles indicate the position of the subharmonic resonance triads from the previous section and vertical lines close to the abscissa denote the azimuthal mode numbers of the cases with $F \to 0.0$ for one of the secondary waves. Note that the triads found in Sec. III.B usually have an azimuthal mode number with a noninteger value. On a cone, however, only integer values of the azimuthal mode number for instability waves in the linear regime can exist. Thus, it is very likely that only detuned Craik-type resonance triads play a role for transition on a cone.

For the first two spectra in Fig. 20, nonlinear wave interactions are very weak. Hence, these spectra are very similar to the spectrum in Fig. 9b. Farther downstream, the spectra are strongly altered by nonlinear wave interactions. Below the two dominant regions of high amplitudes centered at about $k_c = 21$, "legs" develop, which connect disturbance waves from the two dominant regions with high frequency to disturbance waves with frequency approaching zero. These legs are amplified in streamwise direction through nonlinear wave interactions (compare Figs. 20c and 20d). It appears as if the cases with $F \to 0.0$ for one of the secondary waves (see previous section) predict the position of these legs for small frequencies closely (vertical dashed-dotted lines in Figs. 20c and 20d). The circles that reflect the positions of subharmonic resonance growth are located within those legs. Hence, the new resonance triads, where the secondary waves have no subharmonic frequencies, could explain the development of the legs in Figs. 20c and 20d.

Additional to the legs, "ears," which are higher-harmonics in azimuthal direction of the high-amplitude regions, develop at $k_c \sim \pm 55$. These ears are also amplified in streamwise direction and the center region of those ears reach amplitude levels that are comparable in magnitude to the amplitude levels of the legs. Oblique breakdown could explain the appearance of such ears because their center region is nearby the position where one could expect mode [1, 3] of oblique breakdown when a primary wave with $f^* = 23.415$ kHz and $k_c = 21$ is considered. Note that the notation $[n, k]$ is used in oblique breakdown simulations to identify a particular wave according to its frequency n and its azimuthal mode number k. n denotes multiples of the fundamental frequency and k multiples of the smallest azimuthal mode number. Typically, in these oblique breakdown simulations (see also Mayer et al. [5,7] and Laible et al. [25]), the oblique wave pair [1, ±1] is initially forced and the nonlinear development of this wave pair exhibits a characteristic feature [1,8]: Modes with odd azimuthal numbers k are only generated for odd harmonic frequencies n, and modes with even spanwise wave numbers are generated only for even frequencies n. Hence, a signature feature for the initial nonlinear stage of oblique breakdown is the strong growth of the steady modes [0, ±2] and wave modes [1, ±3]. As illustrated in Fig. 20d, the legs at about $k_c \sim \pm 40$ approach an azimuthal mode number where modes [0,

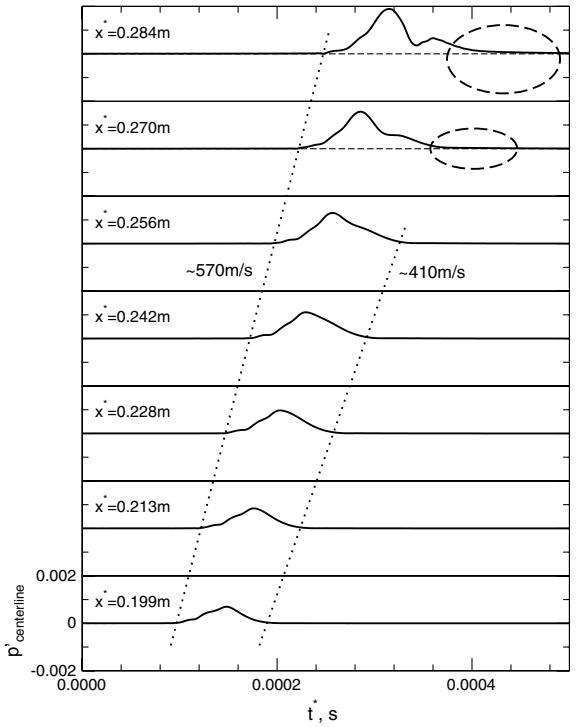

Fig. 22 Temporal evolution of wall pressure envelope for different streamwise positions along the centerline of the wave packet initiated by a high-amplitude pulse. Dotted lines (. . .) are an estimate for propagation speed of the front (∼570 m/s) and the tail (∼410 m/s) of the wave packet. Ellipses highlight a significant change in the packet spreading.

±2] would be if the flow were forced periodically, while the ears can be linked to modes [1, ±3]. It is important to note that in typical oblique breakdown simulations mode [0, ±2] is a truly stationary mode whereas modes within the corresponding peak (legs) in the spectrum of the wave packet have a very low frequency unequal to zero and hence, are not stationary.

Figure 21 shows a very interesting result from a study performed in parallel to the present work (same flow parameters), which addresses the question whether an increasing number of primary disturbance modes can influence oblique breakdown. In this study, Laible et al. [25] force several pairs of oblique instability modes with different frequencies and amplitude levels corresponding to linear *N*-factor

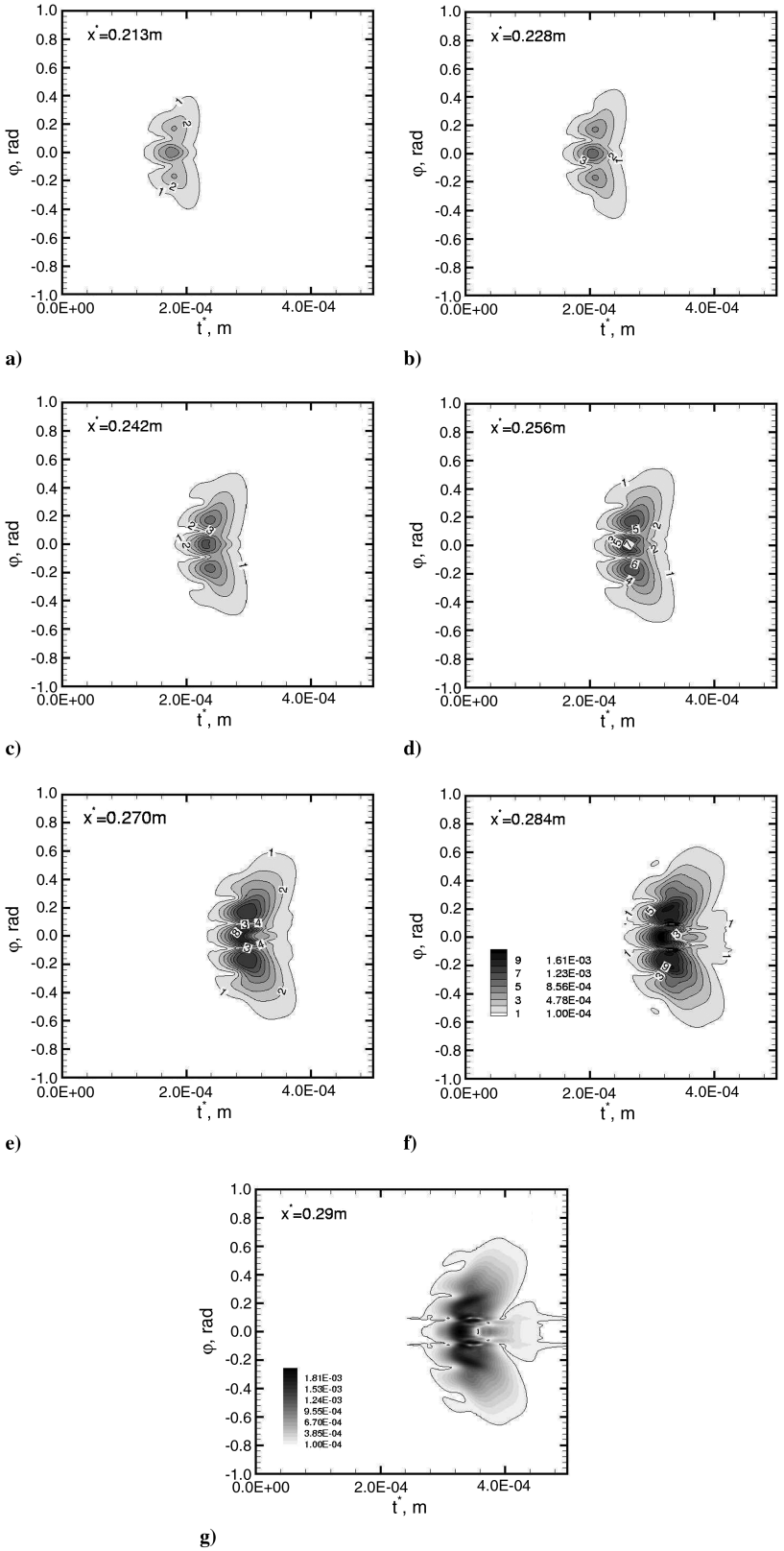

Fig. 23 Temporal evolution of contours of constant amplitudes (envelopes) from wall pressure for different azimuthal angles φ at several streamwise positions from the simulation with the high forcing amplitude. Figures (a)–(f) use the same contour levels.

calculations by prescribing their linear eigenfunctions and a random phase at the inflow. The disturbance spectrum for one of these simulations (case B) at three different streamwise positions is demonstrated in Fig. 21. Note that these spectra are farther downstream than the spectra discussed in this paper. Furthermore, k denotes multiples of the azimuthal mode number $k_c = 32$, which is the azimuthal mode number for the instability waves with the highest streamwise growth (according to N-factor calculations). At $x = 1.65$ (x is nondimensionalized with the cone length of 0.3556 m), two dominant regions of high amplitudes are clearly visible for k unequal to zero. These regions generate legs and peaks in a staggered pattern typical for oblique breakdown farther downstream. When compared with the spectra in this paper, Fig. 21 exhibits two major similarities: 1) the generation of legs at $k = 2$ that end in the steady mode [0, 2] and 2) the generation of mode [1,3]. This comparison confirms that oblique breakdown may also be present in the high-amplitude wave packet from this paper.

To close this section, different features of the wave packet in the weakly nonlinear regime are displayed using envelopes. Figure 22 is very similar to Fig. 12 and differences between the weakly nonlinear stage and the linear transition regime can be immediately observed by comparing both figures. The dotted lines indicate the propagation speed of the front and the tail of the packet. Initially, for the simulation with the higher forcing amplitude the propagation speeds of both, the front and the tail, are very close to the values for the linear regime. Note that the values in Fig. 12 and 22 are only estimated. Also the shape of both packets with different forcing amplitudes are comparable for the first four streamwise positions. Farther downstream, starting at $x^* = 0.270$ m, the wave packet with higher disturbance amplitudes experiences, however, a strong change in shape. A second peak develops at the tail and the spreading of the packet significantly increases while the propagation speed of the tail decreases as highlighted by two ellipses for $x^* = 0.270$ m and $x^* = 0.284$ m.

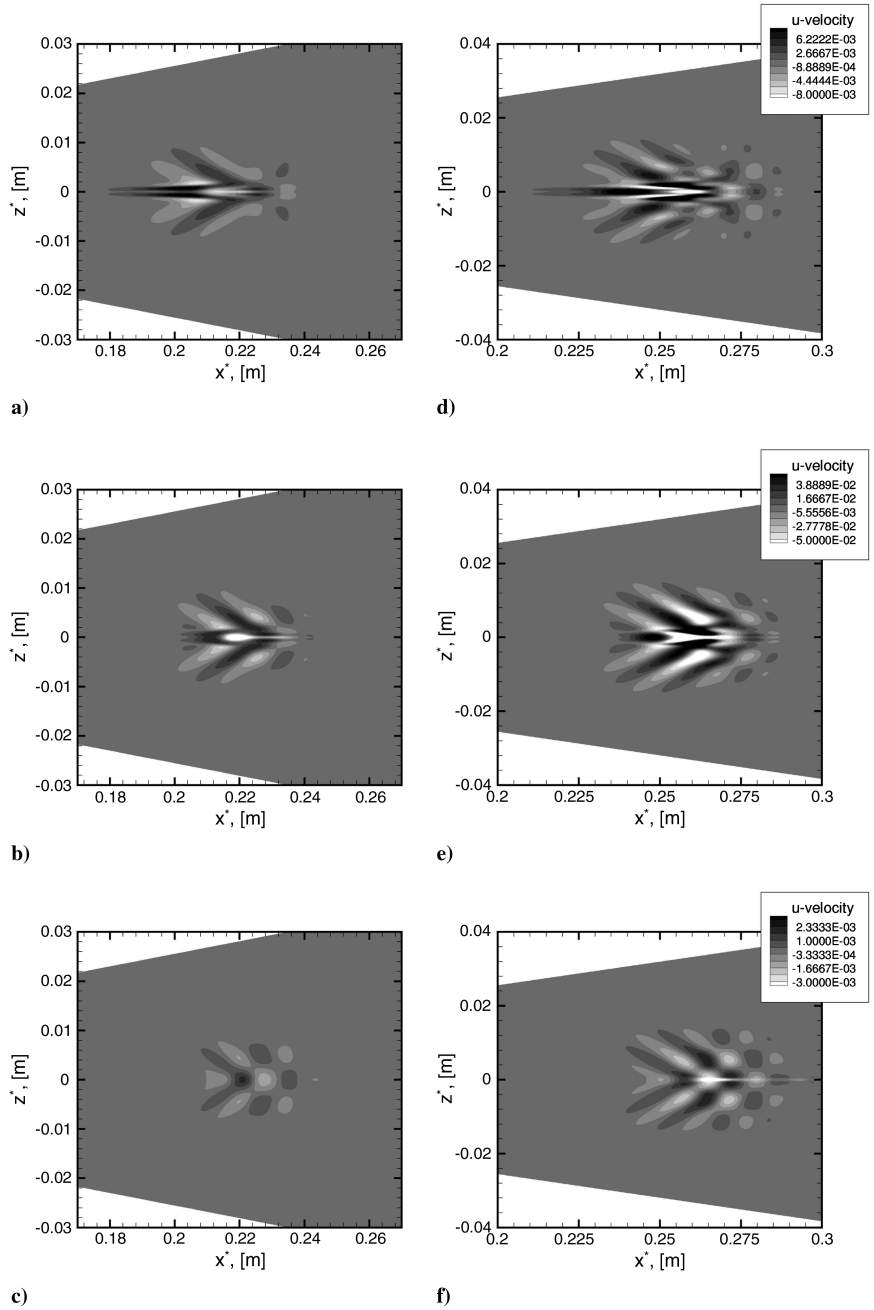

Fig. 24 Spatial evolution of streamwise velocity disturbance u' at different wall-normal positions a) $y^* = 0.125$ mm, b) $y^* = 0.493$ mm, c) $y^* = 0.992$ mm, d) $y^* = 0.125$ mm, e) $y^* = 0.493$ mm, and f) $y^* = 0.992$ mm; and two different time instances: a–c) $t^* = 0.192$ ms and d–f) $t^* = 0.278$ ms.

Figure 23 demonstrates the three-dimensional shape of the wave packet by displaying contours of constant amplitudes (envelopes) from wall pressure for different azimuthal angles φ. This figure gives an impression of how nonlinear wave interactions alter the structures analyzed in Fig. 13. Close to the disturbance hole at $x^* = 0.213$ m, the same butterfly structure as before is visible. With increasing downstream position, this structure is slightly changing when compared with the linear case. The peak on the centerline starts to split in two peaks and longitudinal structures appear between $\varphi = 0.0$ and ± 0.1. These longitudinal structures develop into a pronounced tail for Fig. 23g and cause a significant increase in the spreading of the wave packet. A different view of the wave packet is provided by showing contours of streamwise velocity disturbance at three wall-normal positions in Fig. 24. Close to the wall (Figs. 24a and 24d), two longitudinal structures develop near the centerline. For higher wall-normal positions the influence of these longitudinal structures vanishes. In typical oblique breakdown simulations, a similar behavior can be observed. The streamwise velocity disturbances exhibit features of the steady vortex-mode close to the wall while farther away structures that result from a superposition of the initially forced wave pair are more pronounced.

IV. Conclusions

The spatial and temporal evolution of a wave packet in a cone boundary layer at Mach 3.5 was investigated using LST and DNS. Disturbances were introduced into the boundary layer by pulsing the wall-normal velocity through a hole on the cone surface. The computational setup is very close to experiments by Corke et al. [17] and Matlis [18].

The present study can be divided into three parts. In the first part, the linear development of a wave packet was documented in detail. Contour plots of the wall pressure close to the disturbance hole revealed that three different wave packets were generated by the applied forcing. Two wave packets traveled at a fast group velocity and consisted of disturbances that were damped in streamwise direction. The third wave packet was composed of unstable boundary layer modes that strongly grew in streamwise direction. The latter wave packet was the focus of the present study because this wave packet was assumed to generate transition. The disturbance spectra for this wave packet in the frequency–azimuthal mode number plane based on wall pressure amplitudes exhibited features typical for the linear regime as predicted by LST. Oblique instability modes experienced the highest streamwise amplification. With increasing streamwise position of the disturbance spectra, the highest streamwise amplification shifted to lower disturbance frequencies and higher azimuthal mode numbers. On the unrolled cone surface in the x–z plane, contours of the envelope obtained from the wall pressure showed structures similar to a hand. The number of "fingers" increased in downstream direction.

The second part of the present study focused on the identification of possible, asymmetric resonance triads for the most dominant oblique instability wave of the wave packet. This instability wave has a dimensional frequency of about $f^* \simeq 23.415$ kHz and an azimuthal mode number of about $k_c = 21$ for the present computational setup. With this wave as primary wave of the resonance triads, three different asymmetric, subharmonic resonance triads have been found. Whether these subharmonic resonance triads constitute dominant breakdown mechanisms depends mainly on the following three factors: 1) the linear amplification of all three waves included in the triad, 2) the phase relation between all three waves, and 3) the streamwise change in the azimuthal mode number for the subharmonic waves included in the triads. Furthermore, new resonance triads have been documented where the secondary waves have no subharmonic frequencies. Such resonance triads have not been reported yet for a supersonic boundary layer and therefore, it is unclear if these new resonance triads indeed represent possible transition mechanisms. The study of these new triads, however, suggested that oblique breakdown might be a limiting case of these new resonance triads with one secondary wave having zero frequency. This result can be used to address the question whether oblique breakdown or any other resonance triad is a dominant mechanism in the transition process of a boundary layer at supersonic Mach numbers. The three factors previously mentioned that influence the strength of a resonance interaction, suggest that oblique breakdown is the strongest nonlinear mechanism because both oblique instability waves, initiating oblique breakdown, experience the strongest amplitude growth according to linear theory, and the wave-vortex triad is always synchronized in downstream direction.

Although a study of possible resonance triads based on one dominant instability wave as primary wave is a strong simplification of the real weakly nonlinear development in a wave packet, it might still help with explaining some major findings in the third and final part of the present work. This part focused on the weakly nonlinear development of a large-amplitude wave packet. The initial disturbance development of this wave packet remained linear while farther downstream nonlinear wave interactions altered the shape and the disturbance spectrum of the wave packet. The overall development of the disturbance spectrum obtained from the wall pressure can be summarized as follows:

1) For the present setup, there is no pronounced asymmetric subharmonic resonance in the spectrum although asymmetric subharmonic resonance cannot be ruled out because there is a streamwise growth of disturbance waves that have a subharmonic frequency of the most dominant instability wave in the wave packet.

2) Legs appear at high azimuthal mode numbers in the spectrum that connect instability waves with high frequency to waves with frequency approaching zero. These legs could be explained by the new resonance triads discussed in the second part of this study.

3) Higher-harmonics of the highly amplified oblique instability waves generate ears centered at $k_c \sim \pm 50$ in the wave packet spectrum. These ears might be a result of oblique breakdown. A study performed in parallel (Laible et al. [25]) further corroborates this finding.

Acknowledgments

This research was funded by the Supersonics Project of NASA's Fundamental Aeronautics Program under cooperative agreement NNX07AC66A, with Meelan Choudhari, NASA Langley Research Center, serving as the Technical Monitor. Special thanks to Anatoli Tumin for providing his stability solver. The computer hours and the technical support provided by NASA Ames Research Center are greatly acknowledged.

References

[1] Fasel, H., Thumm, A., and Bestek, H., "Direct Numerical Simulation of Transition in Supersonic Boundary Layer: Oblique Breakdown," *Transitional and Turbulent Compressible Flows*, edited by L. D. Kral and T. A. Zang, Vol. 151, Fluids Engineering Division, American Society of Mechanical Engineers, New York, 1993, pp. 77–92.

[2] Chang, C. L., and Malik, M. R., "Oblique-Mode Breakdown and Secondary Instability in Supersonic Boundary Layers," *Journal of Fluid Mechanics*, Vol. 273, 1994, pp. 323–360. doi:10.1017/S0022112094001965

[3] Jiang, L., Choudhari, M., Chang, C.-L., and Liu, C., "Numerical Simulations of Laminar-Turbulent Transition in Supersonic Boundary Layer," AIAA Paper 2006-3224, 2006.

[4] Mayer, C. S. J., Wernz, S., and Fasel, H. F., "Investigation of Oblique Breakdown in a Supersonic Boundary Layer at Mach 2 Using DNS," AIAA Paper 2007-0949, 2007.

[5] Mayer, C. S. J., and Fasel, H. F., "Investigation of Asymmetric Subharmonic Resonance in a Supersonic Boundary Layer at Mach 2 Using DNS," AIAA Paper 2008-0591, 2008.

[6] Mayer, C. S. J., von Terzi, D. A., and Fasel, H. F., "DNS of Complete Transition to Turbulence via Oblique Breakdown at Mach 3," AIAA Paper 2008-4398, 2008.

[7] Mayer, C. S. J., von Terzi, D. A., and Fasel, H. F., "DNS of Complete Transition to Turbulence via Oblique Breakdown at Mach 3: Part 2," AIAA Paper 2009-3558, 2009.

[8] Thumm, A., "Numerische Untersuchungen zum laminar-turbulenten Strömungsumschlag in transsonischen Grenzschichtströmungen," Ph.D. Dissertation, Universität Stuttgart, Stuttgart, Germany, 1991.

[9] Kosinov, A. D., Semionov, N. V., Shevelkov, S. G., and Zinin, O. I., "Experiments on the Nonlinear Instability of Supersonic Boundary Layers," *Nonlinear Instability of Nonparallel Flows*, edited by D. T. Valentine, S. P. Lin, and W. R. C. Philips, Springer, New York, 1994, pp. 196–205.

[10] Malik, M. R., "Instability and Transition in Supersonic Boundary Layers," *Laminar-Turbulent Boundary Layers*, edited by E. M. Uram, and H. E. Weber, 1984, pp. 139–147.

[11] Mack, L. M., "Stability of Axisymmetric Boundary Layers on Sharp Cones at Hypersonic Mach Numbers," AIAA Paper 1987-1413, 1987.

[12] Gasperas, G., "The Stability of the Compressible Boundary Layer on a Sharp Cone at Zero Angle of Attack," AIAA Paper 1987-0494, 1987.

[13] Fisher, D. F., and Dougherty, N. S., "In-Flight Transition Measurement on a 10° Cone at Mach Numbers From 0.5 to 2.0," NASA TP 1971, 1982.

[14] Beckwith, I. E., Creel, T. R., Chen, F.-J., and Kendall, J. M., "Free Stream Noise and Transition Measurements in a Mach 3.5 Pilot Quiet Tunnel," AIAA Paper 1983-0042, 1983.

[15] Chen, F.-J., Malik, M. R., and Beckwith, I. E., "Comparison of Boundary-Layer Transition on a Cone and Flat Plate at Mach 3.5," AIAA Paper 1988-0411, 1988.

[16] Chen, F. J., Malik, M. R., and Beckwith, I. E., "Boundary-Layer Transition on a Cone and Flat Plate at Mach 3.5," *AIAA Journal*, Vol. 27, No. 6, 1989, pp. 687–693.
doi:10.2514/3.10166

[17] Corke, T. C., Cavalieri, D. A., and Matlis, E., "Boundary-Layer Instability on Sharp Cone at Mach 3.5 with Controlled Input," *AIAA Journal*, Vol. 40, No. 5, 2002, pp. 1015–1018.
doi:10.2514/2.1744

[18] Matlis, E. H., "Controlled Experiments on Instabilities and Transition to Turbulence on Sharp Cones at Supersonic Mach Numbers," Ph.D. Dissertation, Univ. of Notre Dame, Notre Dame, IN, 2003.

[19] Gaster, M., and Grant, I., "An Experimental Investigation of the Formation and Development of a Wave Packet in a Laminar Boundary Layer," *Proceedings of the Royal Society of London*, Vol. 347, No. 1649, 1975, pp. 253–269.
doi:10.1098/rspa.1975.0208

[20] Gaster, M., "A Theoretical Model of a Wave Packet in the Boundary Layer on a Flat Plate," *Proceedings of the Royal Society of London*, Vol. 347, No. 1649, 1975, pp. 271–289.
doi:10.1098/rspa.1975.0209

[21] Medeiros, M. A. F., and Gaster, M., "The Influence of Phase on the Nonlinear Evolution of Wavepackets in Boundary Layers," *Journal of Fluid Mechanics*, Vol. 397, 1999, pp. 259–283.
doi:10.1017/S0022112099006175

[22] Medeiros, M. A. F., and Gaster, M., "The Production of Subharmonic Waves in the Nonlinear Evolution of Wavepackets in Boundary Layers," *Journal of Fluid Mechanics*, Vol. 399, 1999, pp. 301–318.
doi:10.1017/S0022112099006424

[23] Craik, A. D. D., "Non-Linear Resonant Instability in Boundary Layers," *Journal of Fluid Mechanics*, Vol. 50, No. 2, 1971, pp. 393–413.
doi:10.1017/S0022112071002635

[24] Laible, A. C., Mayer, C. S. J., and Fasel, H. F., "Numerical Investigation of Supersonic Transition for a Circular Cone at Mach 3.5," AIAA Paper 2008-4397, 2008.

[25] Laible, A. C., Mayer, C. S. J., and Fasel, H. F., "Numerical Investigation of Transition for a Cone at Mach 3.5: Oblique Breakdown," AIAA Paper 2009-3557, 2009.

[26] Mangler, W., "Zusammenhang zwischen ebenen und rotationssymmetrischen Grenzschichten in kompressiblen Flüssigkeiten," *Zeitschrift für Angewandte Mathematik und Mechanik*, Vol. 28, No. 4, 1948, pp. 97–103.
doi:10.1002/zamm.19480280401

[27] van Leer, B., "Flux-Vector Splitting for the Euler Equations," *International Conference on Numerical Methods in Fluid Dynamics*, Vol. 170, Springer–Verlag, Berlin, 1982, pp. 507–512.

[28] Zhong, X., "High-Order Finite-Difference Schemes for Numerical Simulation of Hypersonic Boundary-Layer Transition," *Journal of Computational Physics*, Vol. 144, 1998, pp. 662–709.
doi:10.1006/jcph.1998.6010

[29] Zhong, X., and Tatineni, M., "High-Order Non-Uniform Grid Schemes for Numerical Simulation of Hypersonic Boundary-Layer Stability and Transition," *Journal of Computational Physics*, Vol. 190, 2003, pp. 419–458.
doi:10.1016/S0021-9991(03)00282-1

[30] Mayer, C. S. J., "Numerical Investigation of the Nonlinear Transition Regime in Supersonic Boundary Layers," Ph.D. Dissertation, Univ. of Arizona, Tucson, AZ, 2009.

[31] Poinsot, T., and Lele, S., "Boundary Conditions for Direct Simulations of Compressible Viscous Flows," *Journal of Computational Physics*, Vol. 101, 1992, pp. 104–129.
doi:10.1016/0021-9991(92)90046-2

[32] Meitz, H., and Fasel, H. F., "A Compact-Difference Scheme for the Navier–Stokes Equations in Vorticity-Velocity Formulation," *Journal of Computational Physics*, Vol. 157, 2000, pp. 371–403.
doi:10.1006/jcph.1999.6387

[33] Balsara, D., and Shu, C.-W., "Monotonicity Preserving Weighted Essentially Non-Oscillatory Schemes with Increasingly High Order of Accuracy," *Journal of Computational Physics*, Vol. 160, 2000, pp. 405–452.
doi:10.1006/jcph.2000.6443

[34] Wang, X., and Zhong, X., "Effect of Wall Perturbations on the Receptivity of a Hypersonic Boundary Layer," *Physics of Fluids*, Vol. 21, No. 4, 2009, pp. 044101–044101-19.

[35] Ermolaev, Y. G., Kosinov, A. D., and Semionov, N. V., "Experimental Investigation of Laminar-Turbulent Transition Process in Supersonic Boundary Layer Using Controlled Disturbances," *Nonlinear Instability and Transition in Three-Dimensional Boundary Layers*, edited by P. W. Duck, and P. Hall, Kluwer Academic, Norwell, MA, 1996, pp. 17–26.

[36] Mack, L. M., "Boundary-Layer Stability Theory," Internal Document 900-277, Jet Propulsion Lab., Pasadena, CA, 1969.

[37] Fedorov, A. V., "Receptivity of a High-Speed Boundary Layer to Acoustic Disturbances," *Journal of Fluid Mechanics*, Vol. 491, 2003, pp. 101–129.
doi:10.1017/S0022112003005263

[38] Tumin, A., "Three-Dimensional Spatial Normal Modes in Compressible Boundary Layers," *Journal of Fluid Mechanics*, Vol. 586, 2007, pp. 295–322.
doi:10.1017/S002211200700691X

[39] Tumin, A., Wang, X., and Zhong, X., "Direct Numerical Simulation and the Theory of Receptivity in a Hypersonic Boundary Layer," *Physics of Fluids*, Vol. 19, No. 1, 2007, pp. 014101.
doi:10.1063/1.2409731

[40] Ma, Y., and Zhong, X., "Receptivity of a Supersonic Boundary Layer over a Flat Plate. Part 1. Wave Structures and Interactions," *Journal of Fluid Mechanics*, Vol. 488, 2003, pp. 31–78.

[41] Eissler, W., and Bestek, H., "Spatial Numerical Simulations of Linear and Weakly Nonlinear Wave Instabilities in Supersonic Boundary Layers," *Theoretical and Computational Fluid Dynamics*, Vol. 8, 1996, pp. 219–235.
doi:10.1007/BF00418059

[42] Balakumar, P., and Malik, M. R., "Discrete Modes and Continuous Spectra in Supersonic Boundary Layers," *Journal of Fluid Mechanics*, Vol. 239, 1992, pp. 631–656.
doi:10.1017/S0022112092004555

[43] Mack, L. M., "Computation of the Stability of the Laminar Boundary Layer," *Methods in Computational Physics*, edited by B. Alder, S. Fernbach, and M. Rotenberg, Vol. 4, Academic Press, New York, 1965, pp. 247–299.

[44] Malik, M. R., and Spall, R. E., "On the Stability of Compressible Flow Past Axisymmetric Bodies," *Journal of Fluid Mechanics*, Vol. 228, 1991, pp. 443–463.

[45] Sivasubramanian, J., Mayer, C. S. J., Laible, A. C., and Fasel, H. F., "Numerical Investigation of Wavepackets in a Hypersonic Cone Boundary Layer at Mach 6," AIAA Paper 2009-3560, 2009.

[46] Craik, A. D. D., "A Model for Subharmonic Resonance Within Wavepackets in Unstable Boundary Layers," *Journal of Fluid Mechanics*, Vol. 432, 2001, pp. 409–418.

A. Tumin
Associate Editor